MNRAS **accepted**, 1–22 (2019) Preprint 25 January 2022 Compiled using MNRAS LATEX style file v3.0

THOR 42: A touchstone ∼24 Myr-old eclipsing binary spanning the fully-convective boundary

Simon J. Murphy,[1,2]★ Warrick A. Lawson,[1] Christopher A. Onken,[2,3] David Yong,[2,4] Gary S. Da Costa,[2] George Zhou,[5] Eric E. Mamajek,[6,7] Cameron P. M. Bell,[8] Michael S. Bessell[2,4] and Adina D. Feinstein[9]†

[1]*School of Science, The University of New South Wales, Canberra, ACT 2600, Australia*
[2]*Research School of Astronomy & Astrophysics, The Australian National University, Canberra, ACT 2611, Australia*
[3]*Australian Research Council Centre of Excellence for All-Sky Astrophysics (CAASTRO)*
[4]*Australian Research Council Centre of Excellence for All-Sky Astrophysics in 3D (ASTRO 3D)*
[5]*Harvard-Smithsonian Center for Astrophysics, 60 Garden Street, Cambridge, MA, 02138, USA*
[6]*Jet Propulsion Laboratory, California Institute of Technology, 4800 Oak Grove Dr., Pasadena, CA 91109, USA*
[7]*Department of Physics & Astronomy, University of Rochester, 500 Wilson Blvd., Rochester, NY 14627, USA*
[8]*Leibniz Institute for Astrophysics Potsdam (AIP), An der Sternwarte 16, D-14482 Potsdam, Germany*
[9]*Department of Astronomy & Astrophysics, University of Chicago, 5640 S. Ellis Ave, Chicago, IL 60637, USA*

arXiv:1911.05925v1 [astro-ph.SR] 14 Nov 2019

Accepted 2019 November 13. Received 2019 November 13; in original form 2019 October 4

ABSTRACT

We present the characterization of CRTS J055255.7−004426 (=THOR 42), a young eclipsing binary comprising two pre-main sequence M dwarfs (combined spectral type M3.5). This nearby (103 pc), short-period (0.859 d) system was recently proposed as a member of the ∼24 Myr-old 32 Orionis Moving Group. Using ground- and space-based photometry in combination with medium- and high-resolution spectroscopy, we model the light and radial velocity curves to derive precise system parameters. The resulting component masses and radii are 0.497 ± 0.005 and $0.205 \pm 0.002\,M_\odot$, and 0.659 ± 0.003 and $0.424 \pm 0.002\,R_\odot$, respectively. With mass and radius uncertainties of ∼1 per cent and ∼0.5 per cent, respectively, THOR 42 is one of the most precisely characterized pre-main sequence eclipsing binaries known. Its systemic velocity, parallax, proper motion, colour–magnitude diagram placement and enlarged radii are all consistent with membership in the 32 Ori Group. The system provides a unique opportunity to test pre-main sequence evolutionary models at an age and mass range not well constrained by observation. From the radius and mass measurements we derive ages of 22–26 Myr using standard (non-magnetic) models, in excellent agreement with the age of the group. However, none of the models can simultaneously reproduce the observed mass, radius, temperature and luminosity of the coeval components. In particular, their H–R diagram ages are 2–4 times younger and we infer masses ∼50 per cent smaller than the dynamical values.

Key words: stars: fundamental parameters — binaries: eclipsing — binaries: spectroscopic — stars: low mass – stars: pre-main-sequence — stars: evolution

1 INTRODUCTION

Understanding the evolution of low-mass stars is an important goal of stellar astrophysics, both observationally and from a theoretical perspective. Not only because M dwarfs constitute the majority of stars in the Solar neighbourhood (∼80 per cent; Henry et al. 2004) but, as they have main sequence lifetimes in excess of a Hubble-time, they can also be used to trace the evolution of stellar properties and the structure of the Galaxy (e.g. Reid et al. 1995; West et al. 2011). Furthermore, their prevalence means they are by definition typical planet hosts and prime targets for ongoing transiting planet searches, for instance by the *Transiting Exoplanet Survey Satellite* mission (*TESS*; Ricker et al. 2015).

However, despite their ubiquity and utility, the properties of low-mass stars (and by extension any planets orbiting them) remain poorly understood, particularly below $\sim 0.35\,M_\odot$ where main sequence stars should have fully-convective interiors (Chabrier & Baraffe 1997). With a few exceptions (e.g. angular diameters from interferometry for the nearest M dwarfs; Boyajian et al. 2012), many of the fundamental properties of low-mass stars are inferred from comparison to evolutionary models, which tabulate stellar parameters (most notably radius, temperature and luminosity) as a function of time at a given mass and chemical composition (e.g. Tognelli et al. 2011; Bressan et al. 2012; Baraffe et al. 2015; Choi et al. 2016). For example, the masses and ages of young

★ E-mail: s.murphy@adfa.edu.au
† NSF Fellow

© 2019 The Authors

Table 1. Properties of J0552−0044. Component parameters derived from the light curve and radial velocity modelling are given in Table 6 and photometry is provided in Table 7.

Property	Value	Ref.
Name	CRTS J055255.7−004426	(1)
2MASS	J05525572−0044266	(2)
Gaia DR2	3218460376351485056	(3)
Right Ascension	05 52 55.732 (ICRS)	(3)
Declination	−00 44 27.031 (ICRS)	(3)
RA proper motion ($\mu_\alpha \cos\delta$)	11.22 ± 0.09 mas yr^{-1}	(3)
Dec. proper motion (μ_δ)	-20.57 ± 0.08 mas yr^{-1}	(3)
Parallax	9.69 ± 0.06 mas	(3)
Distance	102.9 ± 0.6 pc	(4)
Spectral type	M3.5 (combined)	(5,6)
Radial velocity	24.2 ± 0.4 km s^{-1} (systemic)	(5)
Age	24 ± 4 Myr (32 Ori Group)	(5,7)

References: (1) Drake et al. (2014); (2) Skrutskie et al. (2006); (3) *Gaia* DR2 (Gaia Collaboration et al. 2018); (4) Bailer-Jones et al. (2018); (5) This work; (6) Briceño et al. (2019); (7) Bell et al. (2017).

open cluster and moving group members are almost always inferred from comparison to theoretical tracks and isochrones in the Hertzsprung–Russell (H–R) diagram. These cluster ages set the time-scales for the dissipation of circumstellar discs and the formation of planetary systems (e.g. Mamajek 2009; Bell et al. 2013; Murphy et al. 2018). Similarly, our understanding of the stellar initial mass function depends heavily on masses derived from such models (Bastian et al. 2010). As they provide the theoretical backbone to much of contemporary astrophysics, it is therefore imperative that evolutionary models are tested as rigorously as possible against 'touchstone' systems with directly-measured properties (Mann et al. 2015).

Detached, double-lined eclipsing binaries (EBs) are the gold standard for such work. Through detailed photometry and spectroscopy, the masses and absolute radii (as well as temperatures and luminosities) of both components can be derived to few percent precision with minimal model assumptions (Andersen 1991; Torres et al. 2010). EBs therefore provide one of the strongest observational tests of theoretical stellar evolution models available (Stassun et al. 2014; Feiden 2015). Moreover, if an EB is a member of a well-characterized cluster or group, then the models can be calibrated as a function of age. This is especially important at low masses ($\lesssim$0.8 M$_\odot$), where stellar radii contract rapidly with time as stars descend their Hayashi tracks onto the main sequence. Conversely, the dependence of radius on age means EBs can be used in conjunction with models to age-date a stellar population independently of H–R diagram position (e.g. David et al. 2019).

However, despite recent discoveries, particularly from the *Kepler K*2 mission (e.g. Kraus et al. 2015; Lodieu et al. 2015; David et al. 2016a,b; Gillen et al. 2017; David et al. 2019), the census of young EBs remains small. There are currently only 16 known low-mass (<0.8 M$_\odot$) systems of age <1 Gyr with measured masses and radii for both components, of which only nine are younger than the Pleiades (see compilations by Stassun et al. 2014; Gillen et al. 2017; David et al. 2019). The majority of these youngest systems are members of Upper Scorpius (age 5–10 Myr) or the Orion Nebula Cluster (ONC; 1–2 Myr). Moreover, at the lowest masses many systems remain only coarsely characterized, with errors on their component masses or radii of up to ~40 per cent.

In this work we present the precise characterization of a young, double-lined system to add to this census. CRTS J055255.7−004426 (hereafter J0552−0044, Table 1) was first identified as an EB by Drake et al. (2014) in their study of periodic variables in the first data release of the Catalina Surveys (CSDR1). From 192 epochs of pseudo-V-band photometry, they determined a period of 0.858956 d and classified J0552−0044 as an Algol-type detached system. Through comparison to models, Lee (2015) derived the mass, fractional radius and age of eclipsing systems identified by the Catalina Surveys. For J0552−0044 they calculated masses of $M_1 = 0.466 \pm 0.048$ M$_\odot$ and $M_2 = 0.445 \pm 0.052$ M$_\odot$, respectively, and a poorly-constrained system age of 8 ± 24 Gyr. The mass and age ranges of their model isochrones meant they were insensitive to lower-mass components at pre-main sequence ages.

J0552−0044 was proposed as a possible member of the 24 Myr-old 32 Orionis Moving Group (Mamajek 2007) by Bell et al. (2017) (hereafter B17) who noted it was lithium-poor, had a kinematic distance of 92 pc and a UCAC4 proper motion only 2.5 mas yr^{-1} from that expected of a bona fide group member. In addition to the CSDR1 light curve, they presented seven radial velocity measurements and fitted Keplerian orbits at the period found by Drake et al. (2014). The resulting orbital solution had a moderate but statistically-insignificant eccentricity ($e = 0.1 \pm 0.11$). Assuming an edge-on inclination, they derived component masses of 0.438 ± 0.058 M$_\odot$ and 0.164 ± 0.019 M$_\odot$. Given the large photometric errors and poor coverage of the CSDR1 photometry (Fig. 1), they made no attempt to model the light curve and derive radii. With good agreement between the fitted systemic velocity of 20.9 ± 2.3 km s^{-1} and the ~20 km s^{-1} expected of a 32 Ori Group member, B17 considered J0552−0044 a highly likely member pending further velocity measurements and improved photometry.

We have re-examined the spectra presented by B17 and obtained further velocity measurements and photometry covering the full orbit. In Section 2 we review existing photometric observations of J0552−0044 and describe our follow-up photometry and spectroscopy. In Section 3 we jointly model the light curves and radial velocities to derive the properties of the system, including high-precision component masses and radii. In Section 4 we discuss our findings in the context of other young EBs, re-assess membership of J0552−0044 in the 32 Ori Group and compare the system properties to predictions of several evolutionary model grids. We present our conclusions in Section 5.

2 OBSERVATIONS

2.1 Prior photometric surveys

J0552−0044 has been observed by several multi-epoch all-sky surveys, which provide a long baseline of photometry at a variety of cadences. Papageorgiou et al. (2018) recently used the latest Catalina release (CSDR2) to reanalyse stars identified by Drake et al. (2014) as detached EBs, including J0552−0044. Their period agrees with the Drake et al. value to within 1.5 s. V-band photometry is also available from the All-Sky Automated Survey for Supernovae (ASAS-SN; Shappee et al. 2014; Kochanek et al. 2017). Jayasinghe et al. (2019) homogeneously analysed the ASAS-SN light curves of ~412 000 variables from the VSX catalogue (Watson et al. 2006), including J0552−0044. They classified the system as a rotational variable (class `ROT`, probability 51.2 per cent). Karim et al. (2016) presented 60 V-band observations of J0552−0044 (=CVSO 1975) taken over 12 years as part of their ongoing investigation into young stars in Orion. Although the photometry is of poorer quality than Catalina or ASAS-SN, they found a period of 6.08 d which may be an alias (6.08 d/0.8589 d = 7.08). Finally, Heinze et al. (2018) included J0552−0044 in their catalogue of variable stars from the first data release of the Asteroid Terrestrial-impact Last Alert System (ATLAS; Tonry et al. 2018a). ATLAS observed J0552−0044 in two non-standard bandpasses; cyan (4200–6500 Å) and orange (5600–8200 Å). From these data, Heinze et al. classified J0552−0044 as a 'dubious' variable with a period of 1.717864 d (twice the 0.858968 d found here).

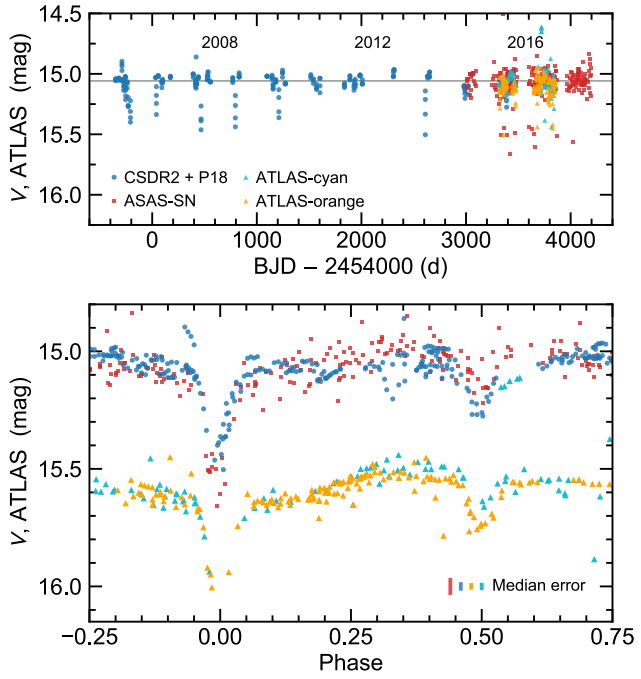


Figure 1. J0552−0044 light curves from the Catalina Surveys (CSDR2; blue points, includes additional photometry from Papageorgiou et al. 2018), ASAS-SN (red points) and ATLAS DR1 (cyan, orange points) phased to the 0.858968 d period found in this work (bottom panel). The Catalina $V_{\rm CSS}$ magnitudes have been shifted to match the median V magnitude from ASAS-SN, while the cyan and orange bandpass ATLAS observations have been shifted by +0.4 and +1.8 mag, respectively. The combined photometric data span ∼13 yr at a variety of cadences (top panel).

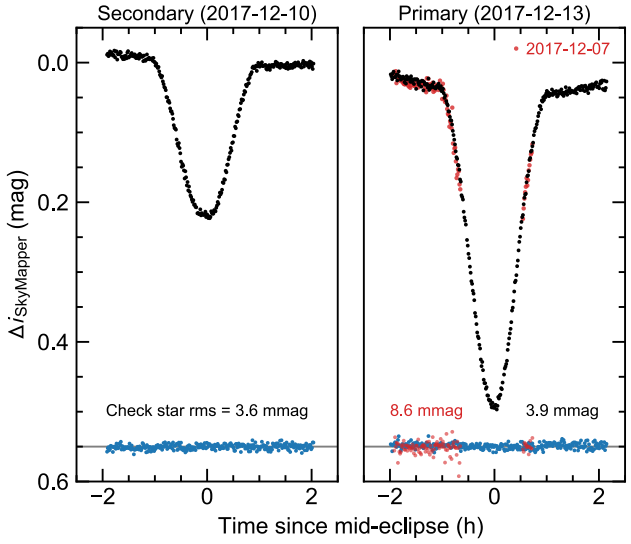


Figure 2. SkyMapper i-band light curves for the secondary eclipse of UT 2017 December 10 (left) and primary eclipse on December 13 (right). The noisier partial primary eclipse on December 7 (red points) was not used in the analysis. The check star at the bottom of each panel is the difference between a single comparison star and the mean of the other two.

We plot the CSDR2, ASAS-SN and ATLAS light curves for J0552−0044 in Fig. 1. Both eclipses are visible, with the secondary eclipse around half the depth of the primary. There is also substantial out-of-eclipse variation, with the secondary eclipse occurring at a brighter baseline than the primary. As the secondary eclipse occurs at phase $\phi \approx 0.5$, the orbital eccentricity must be close to zero (c.f. B17). Unfortunately, the large photometric errors and sparse cadence of these all-sky data mean they are ill-suited for fitting light curve models and determining precise radii. We therefore obtained several dedicated photometric data sets (see Table 2) to better sample the light curve of J0552−0044, which are described below.

2.2 Photometry

2.2.1 SkyMapper 1.3-m

To sample the eclipses at higher cadence and photometric precision we obtained i-band observations on the 1.3-m SkyMapper telescope (Wolf et al. 2018) at Siding Spring Observatory (SSO) on 2017 December 7 (primary eclipse), 10 (secondary) and 13 (primary). Cloud on December 7 prevented the full eclipse from being observed and this noisier partial eclipse was not included in subsequent light curve analysis. The SkyMapper Imager has a field of view of 2.4° × 2.4°, covered by a 268 Mpx camera with 0.5 arcsec pixels. On each night we obtained ∼300 i-band observations extending 2 h either side of the predicted eclipse times. The 30 s exposures and ∼20 s readout time gave a median cadence of 50 s.

The images were processed with a modified version of the Science Data Pipeline (SDP) used for Data Release 2 (DR2) of the SkyMapper Southern Survey (Onken et al. 2019), where the cosmic-ray subtraction was deactivated in order to avoid spurious flagging of electronic noise peaks. The rest of the data reduction proceeded as for DR2: suppression of high-frequency interference noise, overscan subtraction, 2D bias subtraction, per-row bias structure removed by principal components analysis (PCA), flat-field correction, background equalisation between the two amplifiers on each CCD, and a PCA-based subtraction of detector fringing. Photometric zero-points were based on the ATLAS All-Sky Stellar Reference Catalog (Tonry et al. 2018b) after applying Pan-STARRS1-to-SkyMapper bandpass transformations (for details see Onken et al. 2019). In a further modification from DR2 processing, an individual photometric data point consisted of a PSF magnitude determined by a 2D model created from well-measured stars across each CCD using the PSFEX software package (Bertin 2011), where the model was allowed to vary linearly with (x, y) position on the CCD.

We performed differential photometry on these magnitudes using three nearby (<2 arcmin) comparison stars of similar brightness to J0552−0044 to form an unweighted mean comparator and subtracting this from J0552−0044. The resulting eclipse light curves are shown in Fig. 2. The typical uncertainty on the differential magnitudes is 3.8 mmag, which is dominated by a 3.3 mmag error floor on the individual detections from the SDP. As demonstrated by the pseudo-check star, the rms variation of the comparators is $\lesssim$4 mmag, in agreement with the formal uncertainties.

It is apparent from Fig. 2 that the two eclipses are somewhat asymmetric in that the baseline ingress flux is in both cases higher than egress, with this trend not seen in the check stars across either eclipse. Although J0552−0044 is very red ($g - i = 2.54$ mag) compared to most stars in the field (including the comparison stars, see Fig. 4), other stars of similar $(g - i)$ colour in the same exposures show no discernible trend. This seemingly rules out differential atmospheric extinction, which in any case should be small due to the moderate airmass of the observations ($1.15 < \sec z < 1.5$). That a very similar trend appears across a primary and secondary eclipse separated by half an orbit, and is not visible in the other light curves (see below), suggests the cause is observational and not intrinsic to the system (e.g. synchronized spot modulation). In the absence of a physical explanation we mitigate the effect by fitting a quadratic zero-point in time across each night, as discussed in Sec. 3.1.

2.2.2 LCOGT 2-m

We also obtained 40 h of observing time on the Las Cumbres Observatory Global Telescope network (LCOGT; Brown et al. 2013),

Table 2. Summary of J0552−0044 follow-up photometry.

Telescope	Date (UT)	Number of observations	Bandpass	Exposure time (s)	Cadence (s)	Median error (mmag)
SkyMapper 1.3-m (SSO)	2017 Dec 10, 13	581	$i_{\rm SkyMapper}$	30	50	3.8
LCOGT 2-m (Haleakalā)	2018 Jan 14 – 2019 Jan 7	3312	$i_{\rm LCOGT}$	20, 30	35, 45	1.3
TESS (Sector 6)	2018 Dec 15 – 2019 Jan 6	821	6000–10 000 Å	1440	1800	1.8

Table 3. Summary of J0552−0044 spectroscopic observations.

Telescope/instrument	Date (UT)	Resolution ($\lambda/\Delta\lambda$)	Wavelength range (Å)	Exposure time (s)	S/N$^a_{\rm H\alpha}$
ANU 2.3-m/WiFeS (65 epochs)	2015 Oct 23 – 2018 Apr 11	7000	5280–7050	1800^b	150
ANU 2.3-m/WiFeS	2017 Dec 10	3000	3400–9700	2100	200
	2017 Dec 11			1200	140
Magellan/MIKE (0.7 arcsec slit)	2017 Nov 27	35 000 (blue) / 27 000 (red)	3300–9400	300	30
	2017 Nov 28			600	40
	2018 Mar 10			900	60
	2018 Mar 11			900	60
Magellan/MIKE (0.35 arcsec slit)	2018 Mar 2	83 000 (blue) / 65 000 (red)	3300–9400	1800	30
	2018 Mar 4			1200	15

[a] Approximate signal-to-noise ratio per pixel measured around Hα.
[b] Typical exposure time (49/65 exposures).

split between 2-m telescopes at Haleakalā and SSO. Each telescope has a 10.5×10.5 arcmin field of view and is serviced by a 4096×4096 pixel imager with 0.3 arcsec pixels at the default 2×2 binning. In this work we used only the Haleakalā data as it has full phase coverage, better seeing and generally smaller photometric errors than SSO. We observed for a total of 27 nights from Haleakalā, yielding 3809 i-band images. Exposure times were 20 s (30 s for early 2018 data) with a median cadence of 35 s (45 s). Dark current, bias and flat-field reduced images were automatically generated by the LCOGT BANZAI data reduction pipeline (McCully et al. 2018) at the end of each night using the best-available calibration frames. The pipeline also fits an astrometric solution to every image and extracts object fluxes using an adaptive Kron-like elliptical aperture around each source. Rejecting images with poor transparency, large photometric errors or obvious low-level flares, we retained 3312 observations from 18 nights. We then performed differential photometry on J0552−0044 as for the SkyMapper images.

The final LCOGT light curve is plotted in Figs. 3 and 9. The piecemeal cadence in Fig. 3 is the result of balancing the desire for the longest observing blocks possible against the constraints of the automated LCOGT scheduler and its other high priority targets. Blocks were generally limited to $\lesssim$4 h duration within a night. The check stars have an rms of 3–4 mmag, significantly more than the typical 1.0–1.5 mmag uncertainties derived by the pipeline. To ensure we were not underestimating the errors when fitting the light curve model, we fitted a 'jitter' term which is added in quadrature to the formal uncertainties before evaluating the model likelihood (see Sec. 3.1 for more information).

2.2.3 *Transiting Exoplanet Survey Satellite (TESS)*

J0552−0044 was observed by the *TESS* mission (Ricker et al. 2015) in Sector 6 of its survey of the southern sky. Observations covered orbits 19 and 20 of the mission between 2018 December 15 and 2019 January 6. As well as 2 min cadence light curves of selected targets, the spacecraft combines 900 consecutive 2 s exposures to create 30 min cadence Full-Frame Images (FFIs) with a scale of 21 arcsec px^{-1} and an effective exposure time of 24 min after on-board cosmic ray mitigation (Vanderspek et al. 2018). Sector 6 contains 993 FFIs for each camera/CCD combination. The broad *TESS* bandpass is centred on ~8000 Å and has a FWHM of approximately 4000 Å.

We used the ELEANOR software package (v0.2.4; Feinstein et al. 2019) to download and background-subtract a 13×13 (4.5×4.5 arcmin) Target Pixel File centred on J0552−0044 (Fig. 4) suitable for aperture photometry. While the presence of four bright stars ($\Delta G < 1$ mag) within 1–2 arcmin of J0552−0044 is useful for differential photometry (e.g. SkyMapper, LCOGT), the large *TESS* pixels mean a large aperture will be contaminated by flux from neighbouring stars, diluting the eclipses. We therefore chose to use a custom aperture containing the flux of the brightest central pixel only. The light curve was then corrected in ELEANOR for systematic trends by regressing against the three most significant co-trending basis vectors (CBVs) for Sector 6, as produced by the *TESS* Science Processing Operations Center (SPOC) pipeline and convolved down from the short cadence data.

To correct for any remaining systematics and normalize the fluxes, we fitted a low-order polynomial in time to the relatively constant points around secondary eclipse (blue points in Fig. 5) for each orbit and divided it into the light curve. Prior to the fit we masked out poor quality cadences (`quality > 0`; provided in ELEANOR), images affected by flares (see Fig. 5) and any obvious outliers. We also masked out several days at the end of orbit 19 and beginning of orbit 20 ($1475 < \mathrm{TBJD}^1 < 1479$) where the background changed rapidly as the Earth rose above the spacecraft sunshade. The resulting light curve has 821 epochs and a median uncertainty of 1.6 parts per thousand (ppt). The standard deviation of fluxes around secondary eclipse is ~2.7 ppt, suggesting the errors provided by the *TESS* pipeline are underestimated for this pixel and a jitter term may be necessary in the light curve fitting.

The SkyMapper, LCOGT and *TESS* observations are summarized in Table 2. Time-series photometry for J0552−0044 is listed in Table 4. Mid-exposure times are given as Barycentric Julian Dates (BJD) on the Barycentric Dynamical Time (TDB) time-scale. The normalized *TESS* fluxes have been converted to magnitudes as $-2.5 \log(\mathrm{flux})$ and all the light curves shifted so that observations around secondary eclipse have $\Delta m \approx 0.0$.

[1] *TESS* BJD (TBJD) = BJD − 2457000

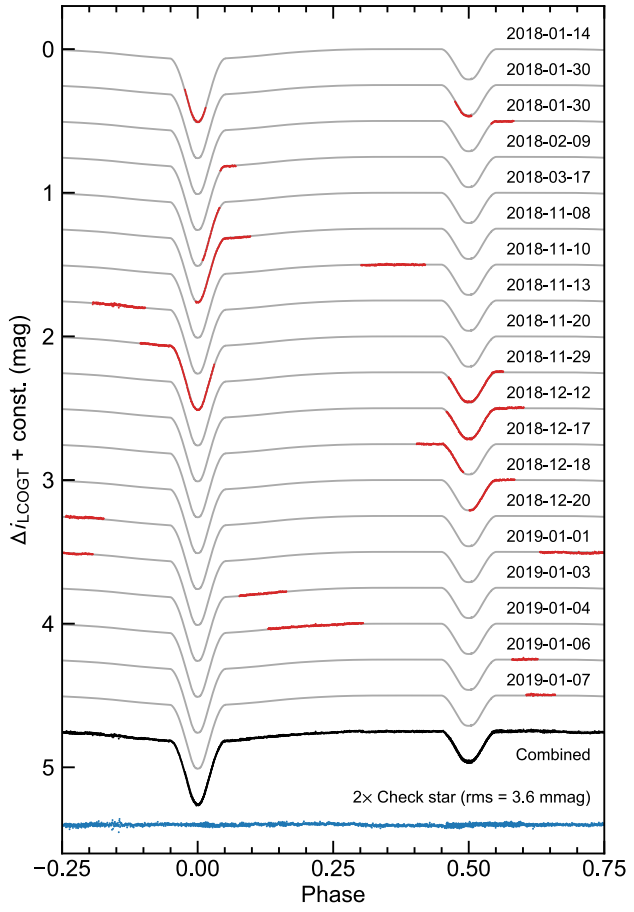


Figure 3. Phased LCOGT i-band observations from 2018/19 (red points). The full light curve is plotted in black; grey lines show the light curve model fitted to the phased data from Sec. 3.1. The check star is calculated as in Fig. 2 but has been scaled by a factor of two here for clarity.

Table 4. Photometry for J0552−0044 from SkyMapper, LCOGT and *TESS*.

BJD − 2450000 (d)	Δm (mag)	σ_m^a (mag)
SkyMapper i-band		
8098.04921	−0.0113	0.0038
8098.04980	−0.0128	0.0038
8098.05037	−0.0093	0.0038
8098.05095	−0.0106	0.0038
8098.05152	−0.0160	0.0038
...	...	...
LCOGT 2-m i-band		
8132.89531	0.2818	0.0011
8132.89584	0.2884	0.0011
8132.89636	0.2972	0.0012
8132.89689	0.3072	0.0012
8132.89742	0.3167	0.0012
...	...	...
***TESS* Sector 6**		
8468.28702	−0.0020	0.0018
8468.30784	0.0320	0.0018
8468.32865	0.1696	0.0020
8468.34952	0.2067	0.0021
8468.37034	0.0743	0.0019
...	...	...

Note. This table is published in its entirety in the electronic version of the article. A portion is shown here for guidance regarding its form and content.
[a] Does not include additional uncertainties determined in the joint modelling, which should be added in quadrature.

2.3 Spectroscopy

2.3.1 ANU 2.3-m/WiFeS

With the aim of deriving radial velocity curves for the system, we obtained 65 epochs of medium-resolution spectroscopy over 25 nights using the Wide Field Spectrograph (WiFeS; Dopita et al. 2007) on the ANU 2.3-m at SSO. With the $R7000$ grating and $RT480$ dichroic, the spectra cover a wavelength range of 5280–7050 Å at a resolution of $R \approx 7000$. The first seven epochs were presented in B17 and the reader is directed to that work and Murphy & Lawson (2015) for details on the observing and data reduction. The spectra have full phase coverage, with typically several observations per night and an exposure time of 1800 s (see Table 3).

As described in B17, we measured radial velocities by cross-correlation against M-type standards from the list of Nidever et al. (2002). A second set of absorption lines was not visible in either the spectra or cross-correlation functions (CCFs), implying we detected only the primary component. However, in most cases the H α emission line was clearly resolved, with a strong component at the primary velocity and a weaker component from the secondary, whose intrinsically stronger emission compensated for the overall flux ratio. We therefore fitted the H α profile at each epoch with two Gaussians and a quadratic continuum ±500 km s^{-1} around the rest wavelength. Representative fits are shown in Fig. 6. We fitted the mean velocity, amplitude and width of each component separately. However, when the separation of the components was minimal ($<2\sigma_{\rm tot}$, where $\sigma_{\rm tot}^2 = \sigma_{\rm pri}^2 + \sigma_{\rm sec}^2$) it was necessary to force both Gaussians to have the same width to avoid over-fitting.

Following this prescription we derived radial velocity differences (RV$_{2-1}$) for 52/65 epochs. The remaining observations were close to eclipses ($|{\rm RV}_{2-1}| \lesssim 70$ km s^{-1}) where only a single component was resolved by WiFeS ($c\Delta\lambda/\lambda \approx 45$ km s^{-1}) or in one case differed by nearly 25 km s^{-1} from the expected value. These velocities are listed in Table 5. The primary velocities are the mean and standard deviation against standards observed that run and we have kept the secondary velocities as differences to avoid introducing additional uncertainties. The uncertainty on RV$_{2-1}$ is the formal error on the mean of each Gaussian added in quadrature.

We also observed J0552−0044 using the lower-resolution $B3000$ and $R3000$ gratings and $RT560$ dichroic on UT 2018 December 10 during secondary eclipse ($\phi = 0.52$) and the next night near quadrature ($\phi = 0.77$). This setup gave coverage of the full optical spectrum (3400–9700 Å) at a resolution of $R \approx 3000$. We also acquired a spectrum of the M3.5 standard star GJ 273 (Kirkpatrick et al. 1991) to aid in spectral typing the system. We reduced and combined the blue and red arms in the FIGARO environment (Shortridge 1993) using similar techniques to the $R7000$ data and flux calibrated using nightly observations of the spectrophotometric standard L745-46A. The reduced spectra are shown in Fig. 7. Both epochs of J0552−0044 are almost identical and are very similar to GJ 273. The only significant differences between the stars are the strong Balmer and Ca II H & K (3969/3934 Å) emission compared to GJ 273 and weaker Ca II Infrared Triplet (8498/8542/8662 Å) absorption, which is presumably filled-in due to activity. The strong similarity to GJ 273 confirms that at optical wavelengths the flux is dominated by the primary component and hence we assign a (combined) spectral type of M3.5. Briceño et al. (2019) recently reported the same spectral type for J0552−0044 (=CVSO 1975) from their spectroscopic survey of low-mass stars across Orion.

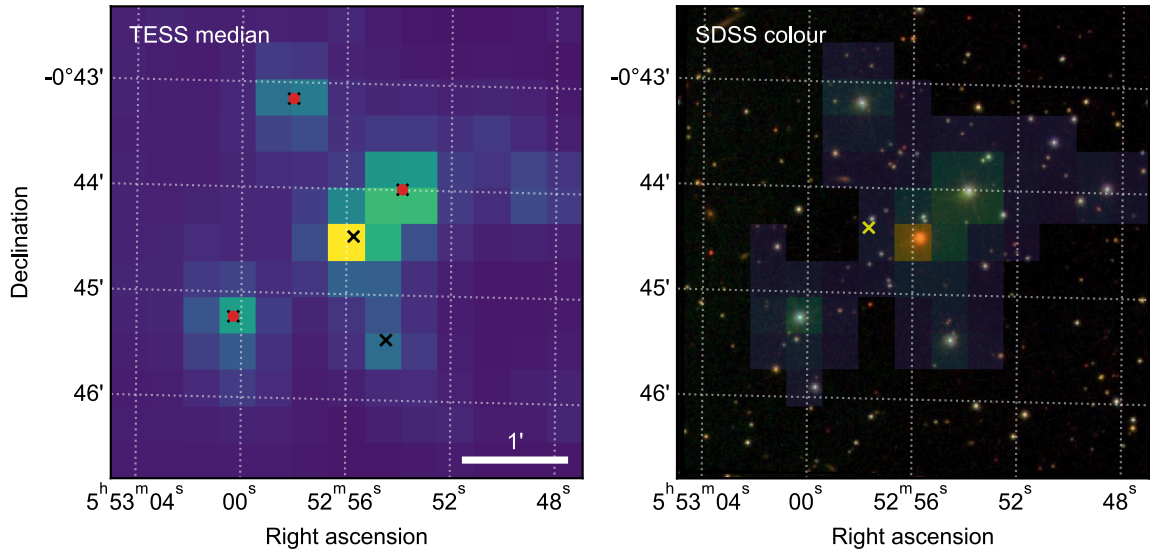


Figure 4. Left: Median 13 × 13 (4.5 × 4.5 arcmin) *TESS* Target Pixel File centred on J0552−0044. The four stars with *Gaia G* within 1 mag of J0552−0044 are shown as crosses; the three used as comparison stars for the SkyMapper and LCOGT photometry are highlighted in red. The fourth star is an unrelated 0.3 d period EB (Drake et al. 2014). Right: Sloan Digital Sky Survey *gri* colour image of the same field with *TESS* pixels overlaid. The yellow cross denotes the position of the *ROSAT* X-ray source 2RXS J055257.6−004422, which we associate with J0552−0044 (see Sec. 3.3).

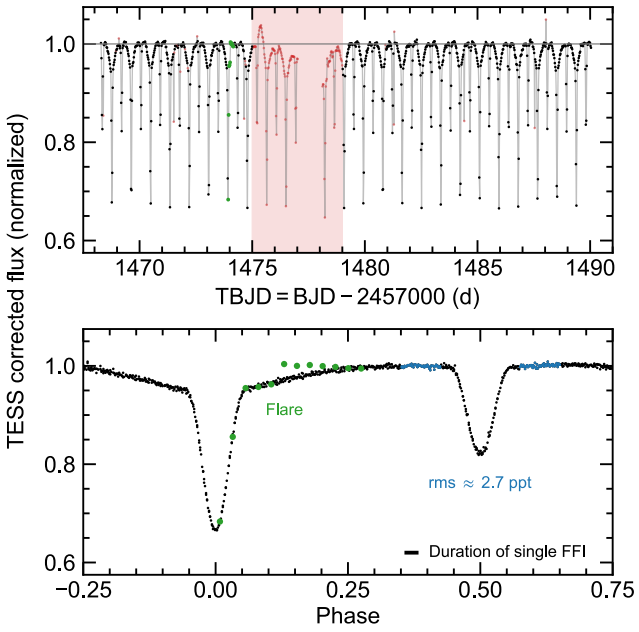


Figure 5. Normalized *TESS* light curve for J0552−0044. Cadences affected by spacecraft momentum dumps or scattered light (red points) were not included in the normalization or light curve fit. Bottom panel: ELEANOR-extracted *TESS* fluxes phased to the 0.858968 d period found in this study. The green points show the progression of a flare observed after primary eclipse on 2018 Dec 21, as traced by the 30 min cadence of *TESS* FFIs.

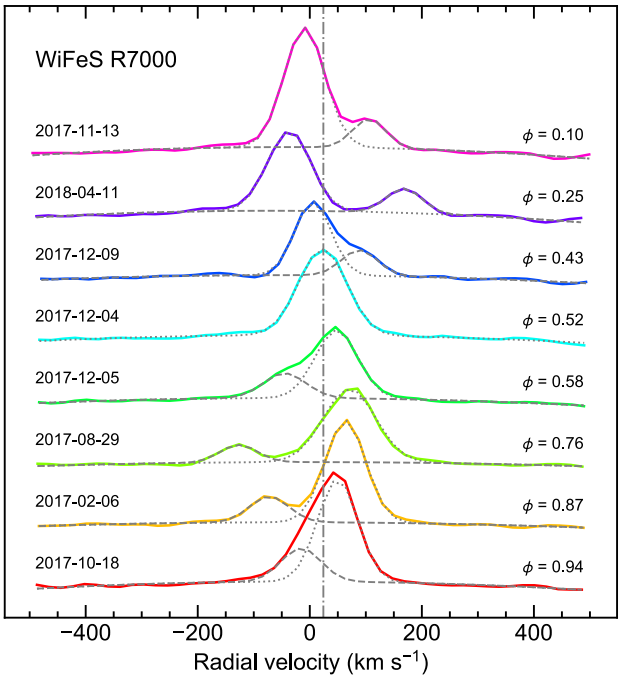


Figure 6. Selected WiFeS/*R*7000 H α emission lines with Gaussian fits to the primary (dotted lines) and secondary (dashed lines) stars as a function of phase ϕ. No secondary was fitted to the $\phi = 0.52$ spectrum at secondary eclipse. The vertical line marks the 24.2 km s^{-1} systemic radial velocity.

2.3.2 *Magellan/MIKE*

Given the short period of J0552−0044, we expect the components to be rotating synchronously (i.e. $P_{\rm rot} = P_{\rm orb} = 0.858$ d). Pre-main sequence models predict synchronous rotation rates of $v \sin i \approx 40$ km s^{-1} for the primary component, which would not be resolved by WiFeS. We therefore obtained six observations of J0552−0044 and GJ 273 using the Magellan Inamori Kyocera Echelle (MIKE; Bernstein et al. 2003) spectrograph on the 6.5-m Magellan Clay Telescope during 2017 November and 2018 March (see Table 3). In most cases we used the 0.7×5 arcsec slit (2× spectral binning, slow readout) which provided a nominal spectral resolution of $R = 27\,000$ in the red arm (4800–9400 Å) and 35 000 in the blue (3300–5000 Å). However, for two epochs (UT 2018 March 2, March 4) we used the 0.35 × 5 arcsec slit (no spectral binning, fast readout) which gave resolutions of 65 000 and 83 000, respectively. The spectra were wavelength calibrated using contemporaneous Th-Ar arcs. We reduced the data following standard procedures in the CARPY pipeline (Kelson et al. 2000; Kelson 2003) to extract and wavelength-calibrate spectra for each of 34 (red) and 36 (blue) echelle orders. No continuum normalization was performed.

We derived radial velocities for the primary component via

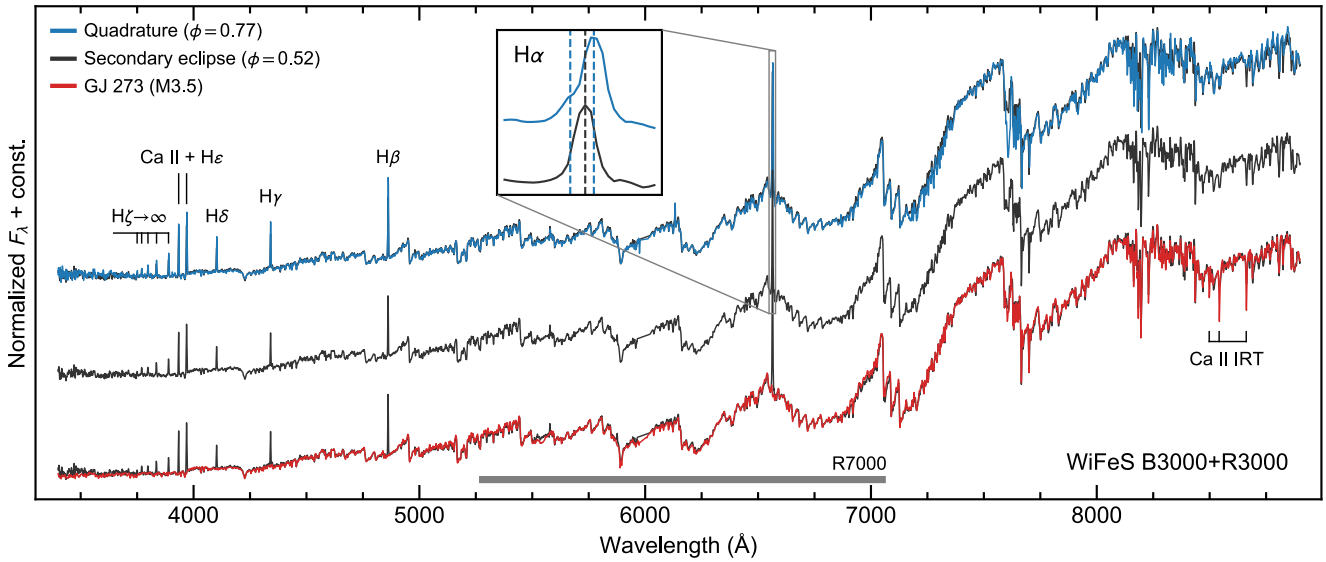


Figure 7. WiFeS/$B3000$ + $R3000$ spectra of J0552−0044 at quadrature (ϕ = 0.77) and secondary eclipse (ϕ = 0.52) compared to the M3.5 dwarf GJ 273. All spectra have been normalized over 7400–7550 Å. The eclipse spectrum is also plotted under the quadrature and GJ 273 spectra for comparison. The inset shows the change in H α emission profile between quadrature and eclipse, with dashed lines marking the positions of the components. The grey horizontal bar gives the wavelength coverage of the $R7000$ spectra. Note the much weaker Ca II Infrared Triplet (IRT) in J0552−0044 compared to GJ 273.

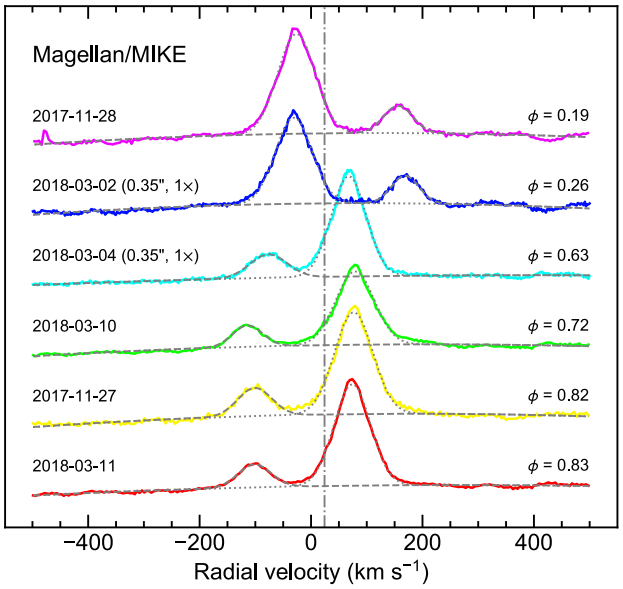


Figure 8. H α emission line profiles with Gaussian fits as per Fig. 6, but for the high-resolution Magellan/MIKE spectra. The two observations taken with the 0.35 arcsec slit and 1× spectral binning are indicated.

cross-correlation against each night's spectrum of GJ 273. We did not obtain a spectrum of GJ 273 on UT 2017 November 27 so in this case used the spectrum from November 28. Each spectrograph arm and order was considered separately and the cross-correlation was performed after fitting and subtracting a low-order polynomial continuum from both stars. Following White & Basri (2003), we fitted the peak of the CCF with a Gaussian and quadratic continuum. Given the broad lines seen in J0552−0044, this was a satisfactory model for most orders. The final mean velocity for each arm was calculated after rejecting telluric-dominated orders with velocities <5 km s^{-1} and performing a 2σ iterative clipping to remove outliers. On the blue side, we did not consider orders <4000 Å due to their lower signal-to-noise ratios and smaller free spectral ranges. Uncertainties for each arm were calculated as the standard deviation across orders. The final velocities at each epoch (see Table 5) are the weighted mean of the red and blue arms after converting to a barycentric frame and adopting a velocity of 18.22 ± 0.1 km s^{-1} for GJ 273 (Nidever et al. 2002). Since only a single peak was visible in the CCFs, we calculated the secondary velocities in the same way as the WiFeS spectra by fitting Gaussians to the H α emission (Fig. 8). H α is visible on two MIKE orders so the final secondary velocities (RV_{2-1}) in Table 5 are the weighted mean of both orders. These velocities agreed to $\lesssim$1.5 km s^{-1} for all six observations.

The Gaussian width of each CCF (σ_{CCF}) encodes the average width of spectral features in that order, which for J0552−0044 we assume have been broadened by the fast rotation of the primary compared to GJ 273. Rotation in GJ 273 has not yet been detected, placing an upper limit of $v \sin i \leq 2.5$ km s^{-1} (Reiners 2007; Browning et al. 2010). Assuming the only broadening observed in GJ 273 is instrumental, we can therefore directly relate σ_{CCF} to $v \sin i$ (White & Basri 2003). We determined the calibration between the two quantities empirically for each order by cross-correlating GJ 273 against a spun-up version of itself over the range $5 < v \sin i < 60$ km s^{-1}. The broadened profiles were constructed using the formalism of Gray (2008) with a linear limb darkening of $\epsilon = 0.6$, and the resulting trend of σ_{CCF} versus $v \sin i$ was well fitted by a cubic polynomial. After excluding orders with velocities outside the calibration range and σ-clipping as above, we calculated mean red and blue $v \sin i$ estimates for each observation, which agreed to <2 km s^{-1}. Uncertainties in each arm were calculated as the standard deviation across orders. From these 12 measurements we calculate a weighted mean of $v \sin i = 37.6 \pm 0.6$ km s^{-1}. The rotation of J0552−0044 is discussed further in Sec. 3.3.

3 ANALYSIS

3.1 Joint light curve and velocity modelling

Having collected light curves and radial velocities, we modelled the physical parameters of J0552−0044 and their uncertainties. To accomplish this we used the Python binary light curve package ELLC (v1.8.4; Maxted 2016)[2], which represents the components of the

[2] https://github.com/pmaxted/ellc

Table 5. Component radial velocities for J0552−0044 from ANU 2.3-m/WiFeS and Magellan/MIKE spectroscopy.

BJD − 2450000 (d)	RV_1 ($km\,s^{-1}$)	$\sigma^a_{RV_1}$ ($km\,s^{-1}$)	RV_{2-1} ($km\,s^{-1}$)	$\sigma^a_{RV_{2-1}}$ ($km\,s^{-1}$)
ANU 2.3-m/WiFeS				
7319.16766	65.5	0.7	−150.8	1.8
7676.17701	−39.3	1.5	197.3	1.7
7760.99193	18.4	1.6		
7761.13840	−34.0	1.0		
7762.01005	−26.4	0.8	187.2	2.6
...	...	...	...	...
Magellan/MIKE (0.7 arcsec slit)				
8084.66078	76.1	0.6	−178.1	0.9
8085.83480	−31.1	1.1	183.2	0.8
8188.50503	79.9	0.7	−192.7	0.8
8188.59845	74.7	0.7	−175.1	0.7
Magellan/MIKE (0.35 arcsec slit)				
8179.52232	−33.0	0.7	200.2	0.5
8181.55586	66.4	0.6	−144.2	0.5

Note. This table is published in its entirety in the electronic version of the article. A portion is shown here for guidance regarding its form and content.
[a] σ_{RV_1} and $\sigma_{RV_{2-1}}$ do not include additional uncertainties determined in the joint modelling, which should be added in quadrature.

binary as triaxial ellipsoids and calculates the observed flux using a combination of Gauss-Legendre integration and exact analytical expressions for the areas of overlapping ellipses which are the projection of these ellipsoids on the sky. As described by Maxted (2016), the flux is calculated from the visible area of the ellipses, which can be calculated exactly, weighted by the average intensity over the visible area, which is estimated by numerical integration over a Cartesian grid defined by the major and minor axes of each ellipse. For efficiency we considered spherical stars with no gravity darkening and adopted the '`very_sparse`' grid which limits the numerical integration to $n = 4$ points along each axis.

Our model comprises 43 parameters to describe the SkyMapper, LCOGT, *TESS*, WiFeS and Magellan data, which are summarised in Table 6. As well as standard parameters describing the stellar radii, disc-averaged surface brightness ratios, reference time, orbital period, eccentricity and inclination, we also included additional parameters to better describe the light curves, radial velocities, star spots and limb darkening, which are detailed below. Note that the orbital semi-major axis, a, is parametrized in ELLC as:

$$a = a_1\,(1 + 1/q) \quad \text{for mass ratio } q = M_2/M_1 \text{ and} \tag{1}$$

$$a_1 \sin i = 0.0197657\,K_1\,P_{\rm orb}\sqrt{1 - e^2} \tag{2}$$

where (a, a_1) are in solar radii, K_1 is in $km\,s^{-1}$, $P_{\rm orb}$ in days, and the numerical factor uses the nominal solar constants given in IAU 2015 Resolution B3 (Mamajek et al. 2015).

3.1.1 *Light curve modelling*

We modelled each photometric data set (SkyMapper, LCOGT, *TESS*) with a zero-point offset and jitter term as free parameters to account for minor normalization differences and underestimated uncertainties. In addition to the constant zero-point term, each SkyMapper eclipse included a quadratic in time to correct the observations for the small trends seen in Fig. 2. Because of the large *TESS* pixels and the possibility the extracted flux was contaminated by neighbouring bright stars, we also included a third light component (ℓ_3) in the *TESS* light curve model (see Maxted & Hutcheon 2018)[3]. For efficiency, we evaluated the full light curve model at every fifth point in the LCOGT time-series, making use of ELLC's ability to linearly interpolate the model at intermediate times. No interpolation was performed between nightly light curve segments. Conversely, we integrated each 1440 s *TESS* observation over 10 subsamples in ELLC to account for the longer exposure time.

3.1.2 *Radial velocities*

We modelled the radial velocity curves in ELLC simultaneously with the light curves as centre-of-mass velocities assuming Keplerian orbits (i.e. ignoring the Rossiter–McLaughlin effect). Secondary velocities were calculated as the RV_{2-1} difference to match the observed Hα offsets in Table 5. Note that this means in effect that the systemic velocities are calculated solely from the primary component. The model also included jitter terms for each of the four data sets and we integrated each observation over 150 s subsamples to account for the non-negligible exposure time (typically 12 samples for an 1800 s WiFeS exposure). To minimize any systematic differences between the WiFeS and MIKE data sets we fitted each with a separate systemic velocity. Furthermore, to mitigate any biases in the primary velocities (which were derived from cross-correlation of photospheric absorption lines) versus the secondary velocities (which originated from chromospheric Hα emission), we also included an additional offset (ΔRV) on the secondary velocities before they were compared to the observations.

3.1.3 *Spot modelling*

J0552−0044 exhibits out-of-eclipse variation, characterized by a broad depression around primary eclipse returning to an approximately flat baseline around secondary eclipse. This is somewhat similar to the reflection/heating effect seen in binaries with hot and cool components, whereby flux from the brighter star (typically an OB star or white dwarf) impinges on the visible disc of the cooler companion (typically an M dwarf). As both components of J0552−0044 are M dwarfs and should differ in temperature by only a few hundred K, we do not expect reflection effects to be significant. Nevertheless, we experimented with various combinations of reflection parameters in ELLC and could satisfactorily replicate the observed light curves. However, these attempts generally required unphysical radii and significant ellipsoidal and/or gravity darkening effects to match the observations, and yielded poor fits to the radial velocities. For instance, given that reflection effects typically produce concave-up light curves around secondary eclipse, with no gravity darkening the model required $R_2 > R_1$ to generate the large ellipsoidal variations at $\phi = 0.25$ and 0.75 necessary to flatten the light curve and replicate the observations.

In light of these deficiencies, we chose to model the out-of-eclipse variation as resulting from the passage of a single dark spot on the surface of the primary (equivalent to a bright spot on the secondary). Spots can naturally explain the light curve modulation and are endemic on low-mass stars. The spot is parametrized in ELLC as a circle with central longitude, latitude, angular radius and brightness ratio ($B_{\rm spot} < 1$ for a dark spot). We assigned each bandpass its own brightness factor in the model. Admittedly, such a simple model is almost certainly a crude approximation to the complex spot patterns present on both stars and their evolution with time. However, toy models show that the net effect is well-modelled by a single, unchanging spot centred near longitude zero (i.e. in line with the secondary as it orbits, see Fig. 12). Both stars are magnetically

[3] The definition of the third light parameter in the latest versions of ELLC is different to the one described in Maxted (2016). See Maxted & Hutcheon (2018) for more information.

Table 6. Fitted and derived parameters from the joint light curve and radial velocity modelling.

Parameter	Symbol	Value	Unit
Eclipse parameters			
Normalized primary radius	R_1/a	$0.1951^{+0.0004}_{-0.0005}$	
Normalized secondary radius	R_2/a	$0.1254^{+0.0003}_{-0.0004}$	
Orbital inclination	i	85.84 ± 0.06	$^\circ$
Eccentricity parameter (f_s)	$\sqrt{e}\sin\omega$	$-0.058^{+0.020}_{-0.012}$	
Eccentricity parameter (f_c)	$\sqrt{e}\cos\omega$	$0.0020^{+0.0014}_{-0.0010}$	
Orbital period	$P_{\rm orb}$	$0.85896804 \pm 0.00000007$	d
Reference time of primary eclipse	t_0	8101.13373 ± 0.00002	BJD−2450000
$i_{\rm LCOGT}$ surface brightness ratio	$J_{\rm LCOGT}$	0.520 ± 0.001	
$i_{\rm SkyMapper}$ surface brightness ratio	$J_{\rm SkyMapper}$	0.541 ± 0.003	
TESS surface brightness ratio	J_{TESS}	$0.577^{+0.003}_{-0.002}$	
Light curve parameters			
$i_{\rm LCOGT}$ zero-point	$\mathrm{ZP}_{\rm LCOGT}$	0.00011 ± 0.00012	mag
$i_{\rm SkyMapper}$ primary eclipse zero-point (constant)	$\mathrm{ZP}_{\rm SkyMapper,P0}$	0.017 ± 0.003	mag
$i_{\rm SkyMapper}$ primary eclipse zero-point (linear)	$\mathrm{ZP}_{\rm SkyMapper,P1}$	-0.096 ± 0.005	mag d^{-1}
$i_{\rm SkyMapper}$ primary eclipse zero-point (quadratic)	$\mathrm{ZP}_{\rm SkyMapper,P2}$	$0.53^{+0.14}_{-0.15}$	mag d^{-2}
$i_{\rm SkyMapper}$ secondary eclipse zero-point (constant)	$\mathrm{ZP}_{\rm SkyMapper,S0}$	$-0.00003^{+0.00075}_{-0.00065}$	mag
$i_{\rm SkyMapper}$ secondary eclipse zero-point (linear)	$\mathrm{ZP}_{\rm SkyMapper,S1}$	-0.094 ± 0.005	mag d^{-1}
$i_{\rm SkyMapper}$ secondary eclipse zero-point (quadratic)	$\mathrm{ZP}_{\rm SkyMapper,S2}$	$0.69^{+0.18}_{-0.20}$	mag d^{-2}
TESS zero-point	ZP_{TESS}	$-0.00004^{+0.00022}_{-0.00019}$	mag
$i_{\rm LCOGT}$ jitter	$j_{\rm LCOGT}$	3.6 ± 0.1	mmag
$i_{\rm SkyMapper}$ jitter	$j_{\rm SkyMapper}$	$0.5^{+0.5}_{-0.3}$	mmag
TESS jitter	j_{TESS}	3.2 ± 0.1	mmag
TESS third-light ratio	$\ell_{3,TESS}$	0.053 ± 0.003	
Radial velocity parameters			
Primary velocity semi-amplitude	K_1	58.0 ± 0.4	km s^{-1}
Secondary velocity semi-amplitude	K_2	140.5 ± 0.7	km s^{-1}
Systemic velocity (WiFeS)	$v_{\rm sys}$	24.2 ± 0.4	km s^{-1}
Systemic velocity (MIKE)	$v_{\rm sys,MIKE}$	$23.9^{+0.5}_{-0.6}$	km s^{-1}
Secondary velocity offset	ΔRV	0.9 ± 0.5	km s^{-1}
Primary velocity jitter (WiFeS)	j_1	3.2 ± 0.3	km s^{-1}
Primary velocity jitter (MIKE)	$j_{1,\rm MIKE}$	$0.8^{+1.0}_{-0.5}$	km s^{-1}
Secondary velocity jitter (WiFeS)	j_2	3.5 ± 0.5	km s^{-1}
Secondary velocity jitter (MIKE)	$j_{2,\rm MIKE}$	$1.9^{+1.0}_{-0.7}$	km s^{-1}
Spot parameters			
Spot central longitude	$l_{\rm spot}$	0.1 ± 0.1	$^\circ$
Spot central latitude	$b_{\rm spot}$	-26^{+2}_{-3}	$^\circ$
Spot radius	$r_{\rm spot}$	39 ± 1	$^\circ$
$i_{\rm LCOGT}$ spot brightness ratio	$B_{\rm spot,LCOGT}$	$0.81^{+0.01}_{-0.02}$	
$i_{\rm SkyMapper}$ spot brightness ratio	$B_{\rm spot,SkyMapper}$	$0.82^{+0.01}_{-0.02}$	
TESS spot brightness ratio	$B_{\rm spot,\,TESS}$	0.82 ± 0.01	
Limb darkening parameters			
$i_{\rm LCOGT}$ triangular sampling parameter 1	$q_{1,\rm LCOGT}$	$0.99^{+0.01}_{-0.02}$	
$i_{\rm LCOGT}$ triangular sampling parameter 2	$q_{2,\rm LCOGT}$	0.12 ± 0.03	
$i_{\rm SkyMapper}$ triangular sampling parameter 1	$q_{1,\rm SkyMapper}$	$0.96^{+0.03}_{-0.07}$	
$i_{\rm SkyMapper}$ triangular sampling parameter 2	$q_{2,\rm SkyMapper}$	$0.20^{+0.05}_{-0.04}$	
TESS triangular sampling parameter 1	$q_{1,TESS}$	$0.74^{+0.10}_{-0.11}$	
TESS triangular sampling parameter 2	$q_{2,TESS}$	$0.05^{+0.08}_{-0.03}$	
Derived parameters			
Primary radius	R_1	$0.659^{+0.002}_{-0.003}$	R$_\odot$
Secondary radius	R_2	0.424 ± 0.002	R$_\odot$
Primary mass	M_1	0.497 ± 0.005	M$_\odot$
Secondary mass	M_2	0.205 ± 0.002	M$_\odot$
Mass ratio (M_2/M_1)	q	$0.413^{+0.005}_{-0.004}$	
Primary surface gravity	$\log g_1$	4.496 ± 0.003	cgs
Secondary surface gravity	$\log g_2$	4.496 ± 0.004	cgs
Orbital semi-major axis	a	3.38 ± 0.01	R$_\odot$
Orbital eccentricity	e	$0.003^{+0.001}_{-0.002}$	
Longitude of periastron	ω	272^{+2}_{-1}	$^\circ$

active and should be synchronously rotating (see Sec. 3.3), so the presence of the companion is likely responsible for the preferential longitude and longevity of the spot pattern.

3.1.4 *Limb darkening*

Rather than constraining the limb darkening coefficients with firm priors or fixing them at values appropriate for the components' temperatures and surface gravities (e.g. Claret & Bloemen 2011; Parviainen & Aigrain 2015), we allowed them to vary as free parameters in the fit. To ensure the quadratic coefficients (u_1, u_2) remained physically bounded, we transformed them to the $q_1 = (u_1 + u_2)^2$ and $q_2 = 0.5u_1(u_1 + u_2)^{-1}$ triangular sampling parametrization proposed by Kipping (2013), with uniform priors on (q_1, q_2) over the interval $[0, 1]$. At each iteration, (q_1, q_2) were transformed back to (u_1, u_2) for use in ELLC. In this way we could derive posterior probabilities on all parameters which fully accounted for our ignorance of the limb darkening profile, yet never explored unphysical solutions. We additionally required that both components share the same (bandpass-dependent) coefficients. As the stars should have similar surface gravities and temperatures, this is a reasonable approach which halves the number of coefficients required.

3.1.5 *Parameter estimation*

We explored the model parameter space using the Markov Chain Monte Carlo (MCMC) ensemble sampler EMCEE (v2.2.1; Foreman-Mackey et al. 2013; Goodman & Weare 2010) to sample the posterior probability distribution of the model and find parameter sets which best describe the observations. At each iteration we calculated the log-likelihood of model parameters θ given the observed data sets $\mathbf{x} = \cup_i x_i$ as follows:

$$\ln \mathcal{L}(\theta|\mathbf{x}) = -\frac{1}{2}\sum_i \chi_i^2 \quad \text{for} \quad i = \text{LCOGT, SkyMapper, } \ldots \tag{3}$$

where the ith data set comprises n observations:

$$\chi_i^2 = \sum_n \ln(2\pi\sigma_n^2) + [\text{obs}_\text{n} - \text{model}(\theta)_\text{n}]^2/\sigma_\text{n}^2 \tag{4}$$

and the uncertainties include a jitter term, j_i, added in quadrature to the observed uncertainties:

$$\sigma_n^2 = \sigma_{\text{obs},n}^2 + j_i^2 \tag{5}$$

We adopted uniform priors on all parameters, imposing physical limits where appropriate. We then sampled the parameter space 100 000 times in EMCEE using 128 walkers. Each walker was initialized from a Gaussian parameter ball around a hand-tuned solution which provided a reasonable fit to the observations. After confirming convergence by inspecting the parameter and posterior probability traces, we conservatively discarded the first 90 000 steps in each MCMC chain as burn-in and report parameter values from the remaining 10 000 steps. The values in Table 6 are the median and $\pm1\sigma$ Gaussian-equivalent uncertainties formed from the 16th and 84th percentiles of the parameter distributions.

The final light curve and radial velocity solutions (corresponding to the median parameters in Table 6) are plotted in Figs. 9, 10 and 11. The single-spot, spherical-star model is able to reproduce the observations with good fidelity, with rms residuals of 3–4 mmag and WiFeS (MIKE) velocity residuals of 3–4 km s^{-1} (1–2 km s^{-1}), in agreement with the input uncertainties and jitter terms. There is some structure visible in the light curve residuals, particularly around the eclipses (Fig. 11). This is likely due to the adopted limb darkening coefficients, which are not well-constrained by the observations and tended to their maximal (q_1) or minimal (q_2) values in the fit. The structure in the LCOGT residuals is dominated by the

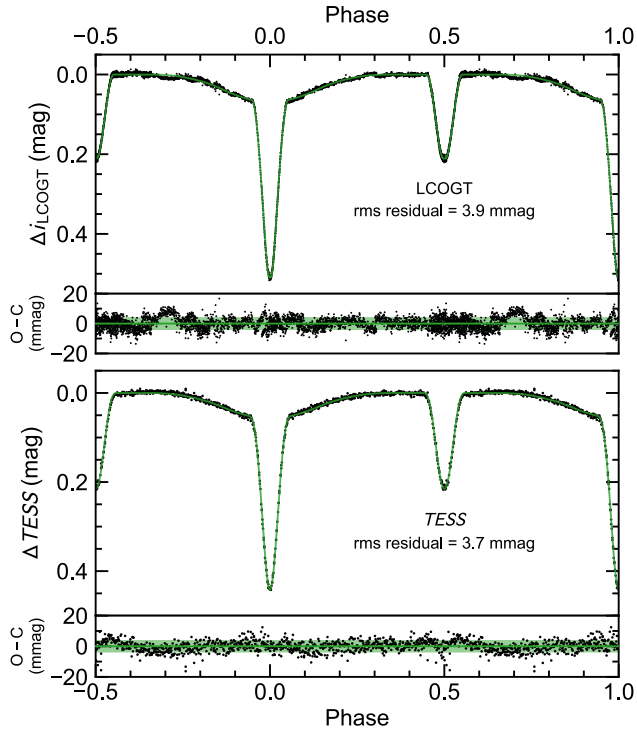


Figure 9. Phase-folded LCOGT and *TESS* light curves for J0552−0044 with the best-fitting model shown in green. Fit residuals are shown in the bottom panel of each plot; the green shaded bars show the rms residual.

effects of combining (uncorrected) light curve segments collected over many nights (Fig. 3).

The modelling yields masses of 0.497 ± 0.005 and 0.205 ± 0.002 $\text{M}_\odot$ for the primary and secondary components, respectively, with radii of 0.659 ± 0.003 and 0.424 ± 0.002 $\text{R}_\odot$. These produce identical surface gravities of $\log g = 4.496 \pm 0.003$ and 4.496 ± 0.004. The mass and radius uncertainties of ∼1 per cent and ∼0.5 per cent, respectively, are well within the 2 per cent convention suitable for the strictest tests of stellar models (Andersen 1991; Southworth 2015). The stars move on tight ($a = 3.38 \pm 0.01\,\text{R}_\odot$; 0.016 au) 0.858968 d orbits which are almost circular ($e = 0.003$). The ratio of stellar radius to effective Roche lobe radius is ∼0.4 for both stars (Eggleton 1983), confirming that the system is detached and the stars are essentially spherical (see below).

The configuration of the system as seen from Earth is depicted in Fig. 12. The secondary is almost entirely occulted at $\phi = 0.5$, which is responsible for the deep secondary eclipse. Interestingly, the spot subtends approximately the same solid angle as the secondary and is fully covered by it at the midpoint of the primary eclipse. As the impact parameter of the eclipse, $b = a\cos(i)/R_1$, depends on the orbital inclination (which is independent of the spot size or stellar radius) it seems unlikely that this configuration is coincidental and must therefore be a consequence of the simple spot model. A spot radius of 39° (covering ∼12 per cent of the stellar surface) is on the high end of inferred sizes reported in the literature for similar systems (e.g. Torres & Ribas 2002; Ribas 2003; López-Morales & Ribas 2005). A more realistic configuration would be smaller, spot complexes with larger brightness contrasts subtending the same approximate surface area as the single spot. Assuming the spot emits thermally, the ∼0.8 brightness ratio corresponds to a temperature ratio of $T_\text{spot}/T_\text{star} \approx 0.95$, in agreement with literature estimates. Further modelling is clearly required to better understand the true spot distribution on both stars. Finally, we note that even if the out-of-eclipse variation is not caused by spot modulation (or is removed prior to fitting; e.g. David et al. 2019), the radii derived from the light curve fit should not be significantly affected.

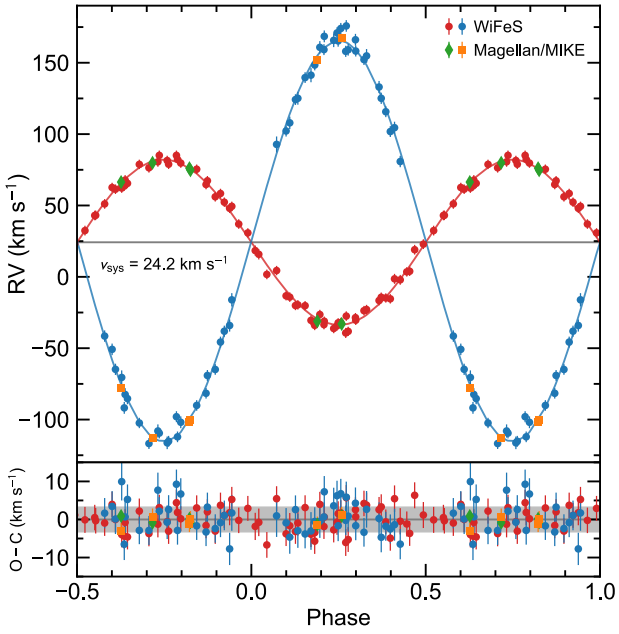


Figure 10. Radial velocity measurements for J0552−0044 from WiFeS (red, blue points) and Magellan/MIKE (green, orange points), with the best-fitting orbital solution given by solid lines. Error bars include the jitter terms added in the fitting. The primary and secondary rms residuals are 3.3 and 4.1 km s^{-1} for WiFeS, and 0.9 and 1.5 km s^{-1} for MIKE, respectively. The grey band in the bottom panel shows the WiFeS primary rms residual.

3.1.6 Robustness of the results

As noted above, to increase the speed of the MCMC analysis we used the sparsest integration grid in ELLC and assumed spherical stars. Here we test the effect these assumptions have on the system modelling. In Fig. 13 we plot the difference between light curves generated from the parameters in Table 6 using the `very_sparse` (n = 4) and `very_fine` (n = 32) integration grids. The largest discrepancy is during the primary eclipse, with the `very_fine` grid giving a 6–7 mmag deeper eclipse at ϕ = 0. By comparison, the fit residuals over the eclipse using the `very_sparse` grid are 3–4 mmag (Fig. 11). Given the large eclipse depth (∼0.45 mag), adopting the sparse grid will therefore result in at most a 1–2 per cent systematic effect on the derived radii.

We also plot in Fig. 13 the difference between light curves generated by spherical stars and those from triaxial ellipsoids assuming Roche geometry. As expected, the ellipsoidal variation is a half-period sinusoid with maxima at ϕ = 0.25 and 0.75. While it may change the inferred spot parameters, the low ∼8 mmag amplitude and minima around the eclipses means that adopting Roche geometry should not significantly affect the radii estimates.

3.2 Spectral energy distribution

From the spectroscopic and light curve analysis we know that J0552−0044's spectral energy distribution (SED) is dominated by the M3.5 primary. To disentangle the contribution from the fainter secondary component we followed the method of Gillen et al. (2017), who analysed EBs in Praesepe and simultaneously fitted the component temperatures, reddening and distance by comparing model fluxes to optical and infrared photometry.

We first gathered photometric observations for J0552−0044 from all available large surveys, noting if the photometry was absolutely calibrated to Vega or the AB magnitude system (or a combination of both, e.g. APASS). We also acquired transmission curves for each bandpass and whether they were tabulated as photon^{-1} or energy^{-1} (for further details see Bessell & Murphy 2012). As no published bandpasses exist for the APASS survey (Henden 2019), we took Johnson B and V transmission curves from Mann & von Braun (2015) and assumed the $griz$ bandpasses were the same as their SDSS equivalents. These observations and references are given in Table 7. We converted each observed magnitude to an in-band flux using either the latest CALSPEC (Bohlin et al. 2014) Vega spectrum[4] or the F_ν = 3631 Jy AB reference spectrum (converted to F_λ through the bandpass pivot wavelength, see Bessell & Murphy 2012). We then computed synthetic fluxes for each bandpass using solar-metallicity BT-Settl (Allard et al. 2012; Baraffe et al. 2015) and PHOENIX v2 (Husser et al. 2013) model atmospheres over a range of effective temperatures 2300 K < $T_{\rm eff}$ < 7000 K and surface gravities 2.5 < log g < 5.5. Before performing the synthetic photometry we linearly interpolated the spectra to

Table 7. Survey photometry of J0552−0044.

Bandpass	Magnitude	System	References
Gaia G	13.911 ± 0.007	Vega	(1,8)
Gaia $G_{\rm BP}$	15.45 ± 0.03	Vega	(1,8)
Gaia $G_{\rm RP}$	12.69 ± 0.02	Vega	(1,8)
SDSS *u*	18.82 ± 0.02	AB	(2,9)
SDSS *g*	16.163 ± 0.004	AB	(2,9)
SDSS *r*	14.793 ± 0.004	AB	(2,9)
SDSS *i*	16.00 ± 0.01[a]	AB	(2,9)
SDSS *z*	12.550 ± 0.004	AB	(2,9)
SkyMapper[b] *g*	15.51 ± 0.01	AB	(3,10)
SkyMapper[b] *r*	14.56 ± 0.01	AB	(3,10)
SkyMapper[b] *i*	12.963 ± 0.005	AB	(3,10)
SkyMapper[b] *z*	12.344 ± 0.004	AB	(3,10)
APASS *B*	16.7 ± 0.1	Vega	(4,11)
APASS *V*	15.17 ± 0.07	Vega	(4,11)
APASS *g*	15.8 ± 0.1	AB	(4,11)
APASS *r*	14.50 ± 0.08	AB	(4,11)
APASS *i*	13.17 ± 0.09	AB	(4,11)
APASS *z*	12.49 ± 0.02	AB	(4,11)
Pan-STARRS *g*	15.68 ± 0.01	AB	(5,12)
Pan-STARRS *r*	14.49 ± 0.01	AB	(5,12)
Pan-STARRS *i*	13.095[c]	AB	(5,12)
Pan-STARRS *z*	12.545[c]	AB	(5,12)
Pan-STARRS *y*	12.158 ± 0.003	AB	(5,12)
2MASS *J*	10.93 ± 0.03	Vega	(6,13)
2MASS *H*	10.29 ± 0.02	Vega	(6,13)
2MASS K_s	10.04 ± 0.02	Vega	(6,13)
All*WISE W*1	9.96 ± 0.02	Vega	(7,14)
All*WISE W*2	9.80 ± 0.02	Vega	(7,14)
All*WISE W*3	9.71 ± 0.05	Vega	(7,14)

[a] Not included in SED fit. Significantly fainter than the SkyMapper, Pan-STARRS and APASS i-band fluxes. SDSS pipeline classifies the i-band detection as a Galaxy.
[b] SkyMapper DR2 photometry is currently only accessible to Australian researchers. The public DR1.1 release is available on VizieR (II/358; Wolf et al. 2018).
[c] Not included in SED fit. No uncertainty given in Pan-STARRS DR2 as all detections are saturated or too extended.
Photometry references: (1) *Gaia* DR2 (Gaia Collaboration et al. 2018); (2) SDSS DR15 (Aguado et al. 2019); (3) SkyMapper DR2 (Onken et al. 2019); (4) APASS DR10 (Henden 2019); (5) Pan-STARRS PS1 DR2 (Chambers et al. 2016); (6) Skrutskie et al. (2006); (7) Wright et al. (2010), Mainzer et al. (2011)
Bandpass references: (8) Evans et al. (2018); (9) SDSS DR7 website (`https://classic.sdss.org/dr7/instruments/imager/filters/index.html`); (10) Bessell et al. (2011); (11) Mann & von Braun (2015), SDSS; (12) Tonry et al. (2012); (13) Cohen et al. (2003); (14) Wright et al. (2010)

[4] CALSPEC name: `alpha_lyr_stis_008`

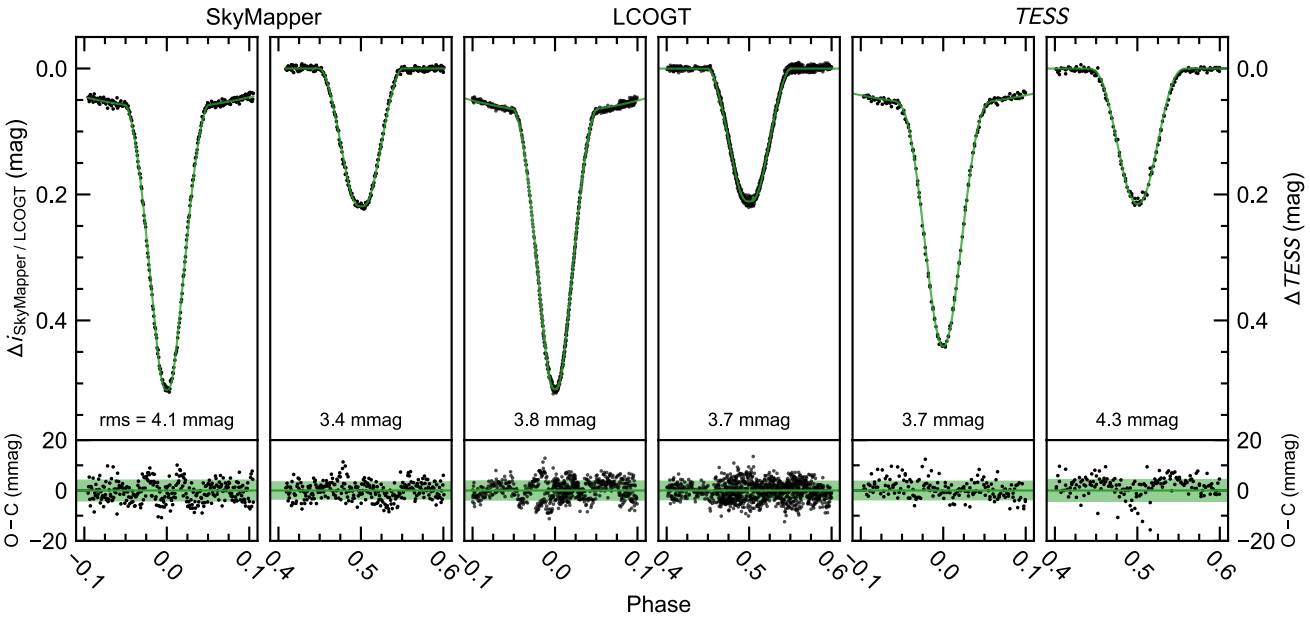


Figure 11. Eclipses of J0552−0044 in each of the three photometric data sets used in this work, with the best-fitting model shown in green. Fit residuals are given in the bottom panel of each plot; the rms residual (green shaded bar) is calculated only for the ranges plotted here. The SkyMapper photometry cover only the eclipses and have been corrected with a quadratic zero-point in time, as described in Sec 3.1.1.

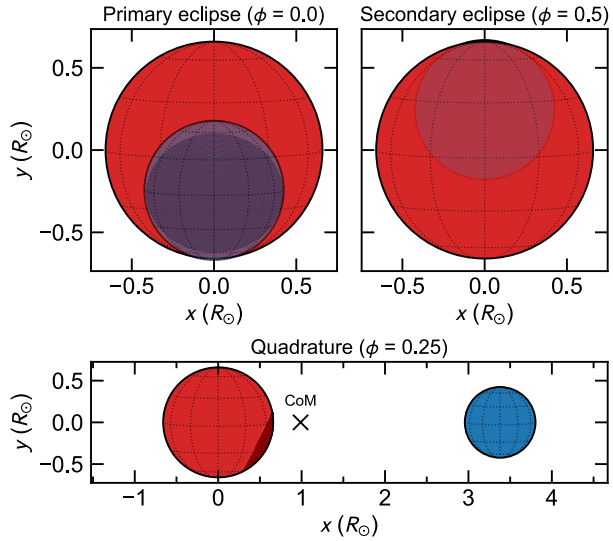


Figure 12. Configuration of J0552−0044 as seen from Earth at primary eclipse, secondary eclipse and quadrature ($\phi = 0.25$). The radii and separation of the components is drawn to scale, with the shaded region on the primary (red) showing the spot inferred in the fitting process. The secondary star (blue) is drawn partially transparent at $\phi = 0$ to show the spot underneath. The centre of mass (CoM) of the system is marked.

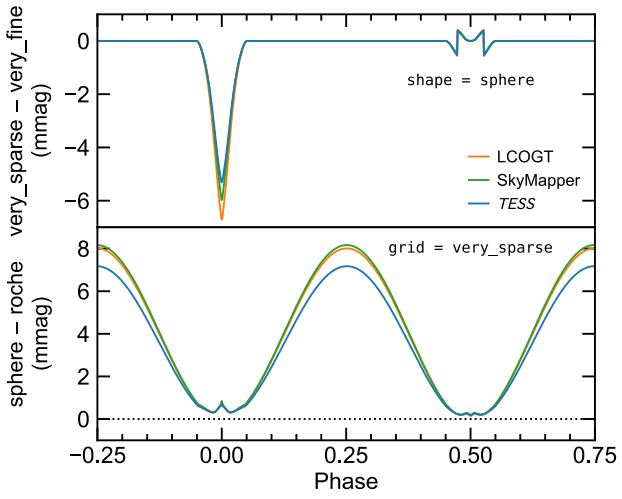


Figure 13. Top panel: light curve difference between the adopted `very_sparse` integration grid and the `very_fine` grid in ELLC for each of the three photometric data sets. Bottom panel: difference between spherical stars and ELLC's Roche ellipsoids. In both panels the light curves were generated using the best-fitting parameters from Table 6.

50 K in $T_{\rm eff}$ and 0.25 in $\log g$. The PHOENIX models only extend to 5 μm and so do not cover the *WISE* $W3$ or $W4$ bandpasses[5].

During the fit the synthetic fluxes, $F(T_{\rm eff}, \log g)$, for each component were linearly interpolated from the model grid, diluted by the factor $(R/d)^2$ for radius R and distance d, reddened to a given $E(B-V)$ and summed to give the combined flux. Note that the reddening vector A_λ is weakly dependent on the underlying stellar SED and magnitude of the extinction. Rather than redden the model spectra we calculated a representative $A_\lambda/E(B-V)$ for each bandpass using a 3300 K, $\log g = 4.5$ BT-Settl model with $E(B-V) = 0.5$ and the extinction law of Cardelli et al. (1989). The free parameters in the fit were therefore the temperature, radius and mass of each component, the distance and the reddening. We also fitted for a photometric jitter term which was added in quadrature to the magnitude errors. This accounts for additional uncertainties not captured by the observations, such as errors in the absolute calibration, the unknown phase of the observations, the effects of spots, etc.

We imposed Gaussian priors on the masses and radii from Table 6 and adopted a *Gaia* DR2 distance prior of 102.9 ± 0.6 pc (Bailer-Jones et al. 2018). With accurate component masses, radii and a distance, the surface gravities and dilution factors are essentially fixed, leaving only the temperatures and reddening to be determined. We adopted uniform priors on the temperatures and a Gaussian prior of $E(B-V) = 0.03 \pm 0.01$ mag on the reddening towards the 32 Ori Group from B17. This minimal reddening agrees with recent 3D reddening maps (e.g. Lallement et al. 2018).

[5] J0552−0044 has an All*WISE* upper limit of $W4 < 8.793$ mag

Table 8. Results of the SED fitting against BT-Settl and PHOENIX model atmospheres. Component masses and radii are not listed as we essentially recover the priors from the joint modelling.

Parameter	BT-Settl	PHOENIX
Primary $T_{\rm eff}$ (K)	3309 ± 22	3284 ± 16
Secondary $T_{\rm eff}$ (K)	3022 ± 13	2992 ± 12
$E(B-V)$ (mag)	0.035 ± 0.01	0.035 ± 0.01
Photometric jitter (mag)	0.19 ± 0.03	0.15 ± 0.03
Distance (pc; *Gaia* prior)	102.8 ± 0.6	102.7 ± 0.6
Distance (pc; uniform prior)[a]	100 ± 5	95 ± 3
Adopted primary $T_{\rm eff}$ (K)	3293 ± 13 (stat.) ± 20 (sys.)	
Adopted secondary $T_{\rm eff}$ (K)	3006 ± 9 (stat.) ± 20 (sys.)	
Primary $\log(L/{\rm L}_\odot)$	−1.337 ± 0.013	
Secondary $\log(L/{\rm L}_\odot)$	−1.879 ± 0.013	

[a] The BT-Settl and PHOENIX temperatures are approximately 20 K and 50 K cooler, respectively, than the *Gaia* prior.

We also imposed a prior on the i-band surface brightness ratio, $J_{\rm LCOGT} = F_2/F_1 = 0.520 \pm 0.001$ which acts as a temperature constraint but is directly related to the observed light curve. We explored the posterior parameter space of the model using EMCEE with 128 walkers and 10 000 steps, conservatively retaining the last half of each chain for parameter estimation.

The results of these fits are presented in Table 8 and the SED of J0552−0044 is plotted against BT-Settl model fluxes in Fig. 14. Both sets of model atmospheres are able to reproduce the observed SED of J0552−0044 with a median reddening slightly larger than the prior. As expected, we recover our tight priors on the masses, radii, surface brightness ratio and distance. We note that the photometric jitter term completely dominates the observed photometric errors in both cases. Like Gillen et al. (2017), we find that the BT-Settl models under-predict the r-band fluxes and give slightly (∼30 K) warmer temperatures than the PHOENIX models, although they agree to within 2σ. Surprisingly, both sets of models over-predict the SDSS u-band flux, where we might expect a young system like J0552−0044 to have enhanced blue emission from its active chromosphere. It is therefore possible that this measurement is erroneous.[6] The other two discrepant blue points in Fig. 14 are the APASS B and SDSS g-band fluxes. Neither is a significant outlier when using the PHOENIX models, but we note that the SDSS g-band magnitude is 0.3–0.6 mag fainter than the SkyMapper, Pan-STARRS or APASS measurements (see Table 7).

We adopt the weighted mean of the BT-Settl and PHOENIX models as our final temperature; this is 3293 ± 13 K for the primary and 3006 ± 9 K for the secondary. The corresponding luminosities from the Stefan–Boltzmann law are $\log(L/{\rm L}_\odot) = -1.337 \pm 0.013$ and -1.879 ± 0.013, where we have included an additional 20 K systematic error on each temperature and used the updated solar constants from Mamajek et al. (2015). The primary temperature agrees with the 3300 K expected of a M3.5 star from the pre-main sequence temperature scale of Herczeg & Hillenbrand (2014), and is bracketed between the Luhman et al. (2003) and Pecaut & Mamajek (2013) predictions of 3340 K and 3260 K, respectively. The Luhman et al. scale is more appropriate for few Myr-old stars with intermediate gravities between dwarfs and giants and so may not be suitable for a system as old as J0552−0044.

As a test we also re-fitted with a uniform distance prior, this gave median distances of 100 ± 5 pc and 95 ± 3 pc for the BT-Settl and PHOENIX models, respectively, with temperatures ∼20 K and ∼50 K cooler than the *Gaia* prior. The good agreement between these distances and the 102.9 pc from *Gaia* shows that the radii inferred from the light curve modelling are accurate. A uniform prior on $E(B-V)$ produced median reddenings of ∼0.2 mag and temperatures 100–200 K warmer than the B17 prior. Such a high reddening is not supported by the 3D maps or the close agreement between the spectra of J0552−0044 and GJ 273 (Fig. 7), which at a distance of 3.8 pc is essentially unreddened.

[6] SkyMapper DR1.1 (Wolf et al. 2018) includes a brighter u-band magnitude of 17.97 ± 0.26 for J0552−0044 from two observations, which is near the faint limit of its Shallow Survey. However, none of these or subsequent observations were of high enough quality for inclusion in DR2.

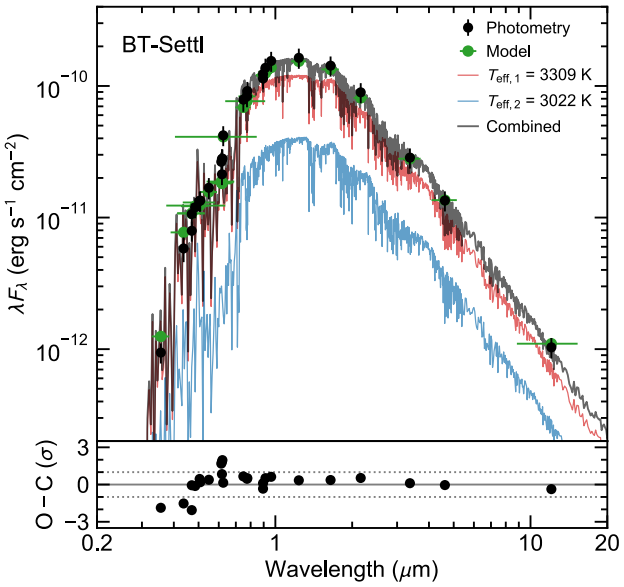


Figure 14. Spectral energy distribution (SED) of J0552−0044 constructed from the magnitudes in Table 7 (black points). The best-fitting BT-Settl model atmospheres for the primary and secondary stars are plotted in red and blue, respectively. Their combined SED is given by the grey line and green points. Horizontal error bars show the equivalent width of each bandpass.

3.3 Rotation and activity

As outlined above, the short period of J0552−0044 implies that the two components should be rotating synchronously and have circular orbits. Using the period (0.858968 d) and mass ratio ($q = 0.41$) derived from the joint modelling, we estimate an approximate synchronization time-scale of ∼16 kyr and a circularization time-scale of 0.6 Myr (Zahn 1977, equations 6.1 and 6.2). Clearly these are both much less than the 24 ± 4 Myr age of the 32 Ori Group (B17) which we ascribe to J0552−0044.

Circularization of the orbits appears to have taken place – our best-fitting eccentricity ($e = 0.003^{+0.001}_{-0.002}$) is consistent with zero, and assuming synchronous rotation we calculate a projected rotation rate for the primary of $v \sin i_{\rm calc} = 38.7 \pm 0.2$ km s^{-1}. The uncertainty reflects the variation in the radius, period and orbital inclination from Table 6. As discussed in Sec. 2.3.2, from the 12 Magellan/MIKE measurements we find a weighted mean of $v \sin i_{\rm obs} = 37.6 \pm 0.6$ km s^{-1}, in excellent agreement with the synchronous estimate. Assuming the out-of-eclipse variability is dominated by spots, the stability of the spot pattern in phase over the ∼1 yr baseline of observations presented here (>400 orbits) is further evidence of synchronicity. The effect of this fast rotation is readily apparent in Fig. 15, where we compare a portion of the MIKE spectrum of J0552−0044 to the slow-rotating template GJ 273 ($v \sin i < 2.5$ km s^{-1}). By broadening the latter we find a best-fitting $v \sin i \approx 38$ km s^{-1} for this region, in agreement with the value derived from the CCF width calibration.

This fast rotation gives rise to enhanced magnetic activity, manifest in J0552−0044 by strong H α and other Balmer line emis-

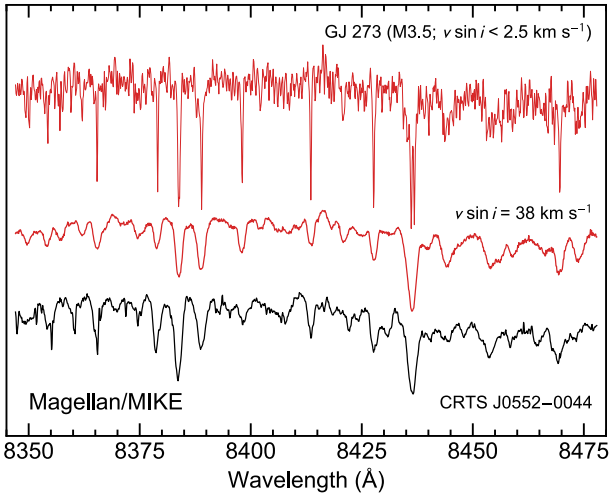


Figure 15. Magellan/MIKE spectrum of J0552−0044 (bottom) compared to the M3.5 slow-rotator GJ 273 (top). By broadening the latter to $v \sin i \approx 38$ km s^{-1} we can reproduce the broad lines observed in J0552−0044. Note the actual determination of $v \sin i$ was made using the cross-correlation function width and not by comparing spectra directly.

sion, Ca II H & K emission and the filled-in absorption lines of Na I D and the Ca II IRT (Fig. 7). It should also produce strong coronal X-ray emission. *ROSAT* detected a point source, 2RXS J055257.6−004422, ∼30 arcsec to the east of J0552−0044 with a positional error of 19 arcsec (see Fig. 4). Assuming this source is associated with J0552−0044[7], we use the count rate and hardness ratio from the Second *ROSAT* All-Sky Survey (2RXS; Boller et al. 2016) and the conversion factor of Fleming et al. (1995) to derive a 0.1–2.4 keV flux of $\sim 3 \times 10^{-13}$ erg cm^{-2} s^{-1}. We note that this detection is near the *ROSAT* faint limit, with errors on the count rate and hardness ratio of ∼30 per cent and ∼100 per cent, respectively. With a system luminosity of $\sim 0.06\,L_\odot$, we find an X-ray to bolometric luminosity ratio of $\log(L_X/L_{bol}) \sim -2.8$, consistent with the $\log(L_X/L_{bol}) \approx -3$ saturated X-ray emission seen in young and active stars (e.g. Fleming et al. 1989; Stauffer et al. 1997). Finally, we note that the 2RXS binned light curve ($\Delta t = 3.2$ h) is consistent with a constant count rate over the ∼44 h baseline of the *ROSAT* observations, with no flares apparent. While a quantitative discussion of flare rate and strength in J0552−0044 is beyond the scope of this work, the detection of several low-level flares in the LCOGT and *TESS* light curves (e.g. Fig. 5) is consistent with the enhanced activity observed in young, low-mass stars and close binaries.

4 DISCUSSION

4.1 J0552−0044 in context

We plot in Fig. 16 our radius and mass measurements compared to the pre-main sequence evolutionary models of Baraffe et al. (2015) (hereafter BHAC15). The components of J0552−0044 are coeval in the mass–radius diagram and have larger radii and lower surface gravities ($\log g = 4.5$) than older field stars of the same mass, as expected of young stars finishing their contraction onto the main sequence. Note that the $\log g = 4.5$ line of constant surface gravity is essentially parallel to the models at these ages. Both components appear slightly older than the 24 Myr BHAC15 isochrone at the canonical age of the 32 Ori Group. After creating a denser set of isochrones ($0 < \log t/\mathrm{Myr} < 2$; $\Delta \log t = 0.02$), a linear interpolation[8] of the models yields ages of 25.4 and 26.2 Myr for the primary and secondary, respectively. We compare the full gamut of system properties (masses, radii, surface gravities, temperatures, luminosities) to the BHAC15 and other contemporary pre-main sequence models in Sec. 4.3.

Also plotted in Fig. 16 is the census of young (<1 Gyr), low-mass (<0.8 $M_\odot$) EBs collated by Gillen et al. (2017) and David et al. (2019). This ensemble provides the best-available constraints on evolutionary models at the lowest masses and ages (e.g. Stassun et al. 2014). J0552−0044 is one of only 17 such systems identified to date and only the second low-mass EB at intermediate ages between young groups like the ONC (1–2 Myr) and Upper Scorpius (5–10 Myr), and older populations like the Pleiades (125 Myr) and Praesepe (∼600 Myr). The other system is NSVS 06507557 (Ćakırlı & Ibanoğlu 2010) which is claimed to have an age of ∼20 Myr. However, its component ages inferred from our mass–radius diagram are inconclusive. The primary lies on the 1 Gyr isochrone while the secondary is about 35 Myr old, with a radius ∼50 per cent larger than its expected main sequence value. The fast-rotating ($P = 0.52$ d) system shows evidence of spot activity and its optical spectrum has Li I absorption as well as Balmer and forbidden line emission characteristic of young stars. It is not a known member of any nearby star-forming region or moving group. There is a faint star 4 arcsec to the south with a nearly identical *Gaia* parallax and proper motion, so it is possible this wide companion has complicated the light curve or velocity analysis, or is responsible for the spectroscopic youth indicators. Regardless of its exact age, the masses derived by Ćakırlı & Ibanoğlu (2010) are not precise enough for stringent testing of evolutionary models.

At higher masses (>0.8 $M_\odot$), J0552−0044 joins the intermediate age systems NP Per (1.3 + 1.0 $M_\odot$, ∼17 Myr; Lacy et al. 2016), MML 53 (1.0 + 0.9 + 0.7 $M_\odot$, 16 Myr; Hebb et al. 2010, 2011; Gómez Maqueo Chew et al. 2019) and several solar-type EBs in the greater Orion OB1 association (Stassun et al. 2014). MML 53 in particular has a well-constrained age from its membership in the Upper Centaurus Lupus subgroup of the Sco-Cen OB association (16 ± 2 Myr; Pecaut & Mamajek 2016).

Low-mass EBs with mass ratios $\ll 1$ are especially valuable for testing evolutionary models as they allow an assessment of the model predictions over a wide range of masses at a single age and metallicity. Among the young systems in Fig. 16, J0552−0044 has one of smallest mass ratios ($q = 0.41$) and is one of only six systems spanning the ∼0.35 $M_\odot$ main sequence fully-convective boundary (Chabrier & Baraffe 1997). The others are NSVS 06507557, RIK 72 (single-lined system; David et al. 2019), and older members of the Pleiades (MHO 9; David et al. 2016a), Praesepe (AD 3814; Gillen et al. 2017) and NGC 1647 (2MJ0446+19; Hebb et al. 2006). J0552−0044 could be considered a younger analogue of 2MJ0446+19, which has a similar orbital period (0.62 d), component masses (0.47 + 0.19 $M_\odot$; $q \sim 0.4$) and temperatures (3320 K, 2910 K). In contrast to NSVS 06507557, the primary component of 2MJ0446+19 (age ∼150 Myr) is significantly inflated while the secondary lies on the 1 Gyr isochrone.

Star formation theories predict that short-period M dwarf binaries with low mass ratios should be rare (Nefs et al. 2013). This is due to primordial factors, such as the nascent secondary preferentially accreting infalling gas with high angular momentum, driving the mass ratio to unity (e.g. Bate 2000; Bate et al. 2002), as well as dynamical effects in the young cluster. Both the dynami-

[7] In their automated catalogue of radio/X-ray associations to optical sources (MORX), Flesch (2016) associated 2RXS J055257.6−004422 with a faint ($R \sim 19.2$ mag) optical source 16 arcsec south-west of the *ROSAT* detection. They note, however, that there is a 56 per cent probability the association is false. Given the positional error on the detection and expectation of copious X-ray emission from a fast rotating young binary, we believe 2RXS J055257.6−004422 is more likely associated with J0552−0044.

[8] Using `scipy.interpolate.LinearNDInterpolator` in PYTHON.

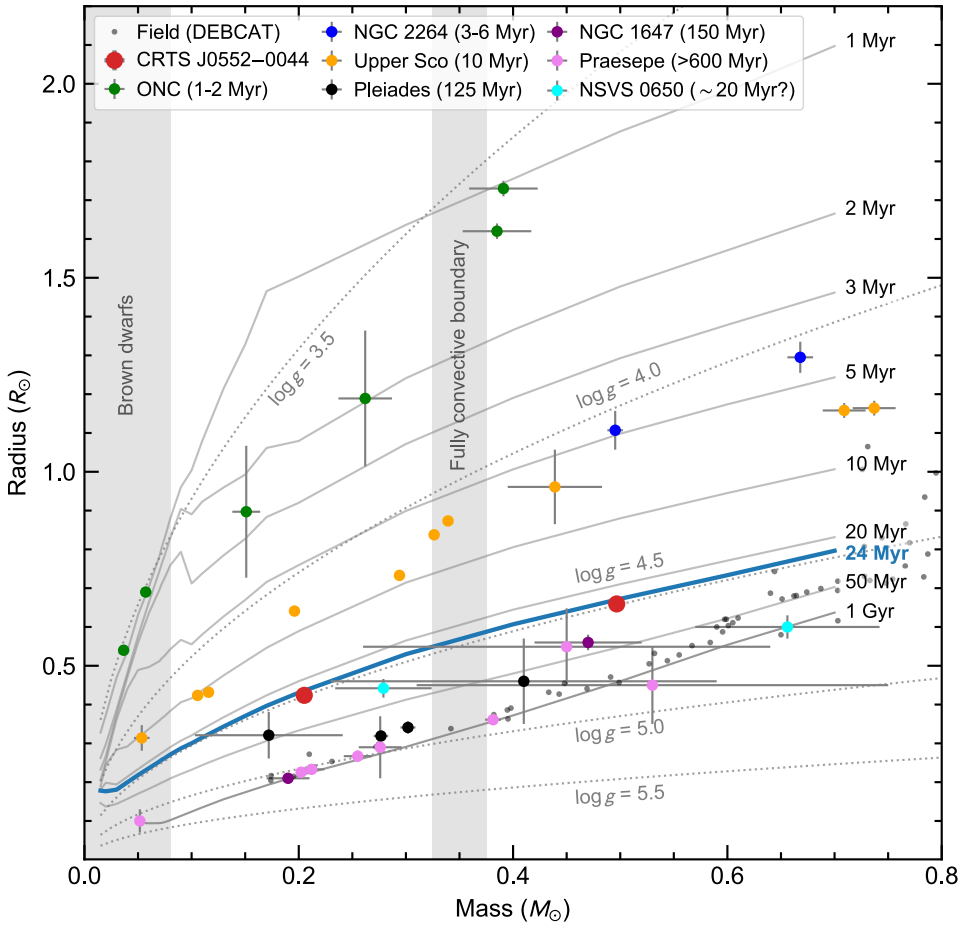


Figure 16. Mass–radius diagram comparing J0552−0044 (large red points; error bars smaller than the point size) to well-characterized field-age EBs (DEBCAT; Southworth 2015) and young (<1 Gyr), low-mass systems collated by Gillen et al. (2017) and David et al. (2019). Note that the Upper Sco star with the largest errors is a single-lined system (RIK 72) with an inferred ∼0.05 $M_\odot$ companion (also plotted). We also include the components of NSVS 06507557 (Ćakırlı & Ibanoğlu 2010), which is claimed to have an age of ∼20 Myr (see text). Overplotted are solar metallicity Baraffe et al. (2015) isochrones (solid lines) and surface gravity contours from $\log g$ = 3.5 to 5.5 (dotted lines). The thick blue line is the 24 Myr isochrone at the age of the 32 Ori Group and the shaded region indicates the boundary between partially and fully-convective ($\lesssim$0.35 $M_\odot$) stellar interiors on the main sequence.

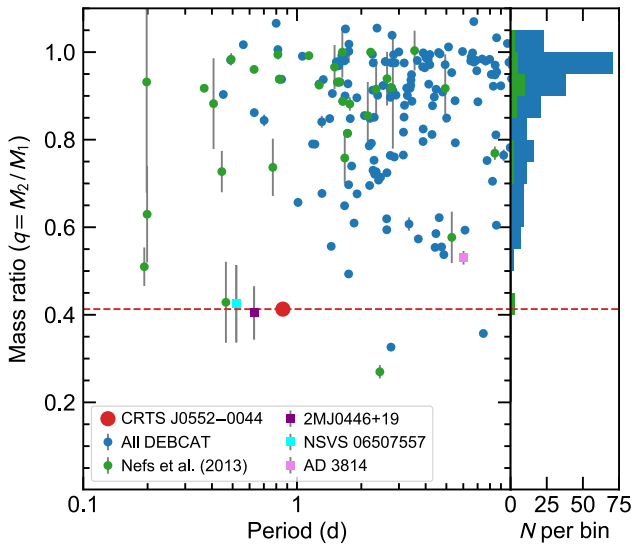


Figure 17. Mass ratio and period distribution of EBs from DEBCAT (blue points; Southworth 2015) and short-period (P < 10 d) M dwarf systems from Nefs et al. (2013) (green points). The three short-period systems from Fig. 16 which span the fully-convective boundary are plotted as coloured squares. The histogram gives the mass ratio distribution for the Nefs et al. stars and the full DEBCAT sample.

cal decay of small-N multiples or exchanges with single stars will tend to tighten orbits and eject the lowest-mass components (e.g. Sterzik & Durisen 1995; Goodwin et al. 2007). The frequency of short-period, unequal-mass binaries is therefore expected to decrease steeply with the mass of the primary.

The present-day result of these processes is illustrated in Fig. 17, where we compare J0552−0044 in period–mass ratio space to the high-precision (mass and radius errors $\lesssim$2 per cent) DEBCAT[9] sample (Southworth 2015) and short-period (P < 10 d) M dwarf binaries collated by Nefs et al. (2013). While the majority of systems have mass ratios close to unity, J0552−0044 falls in a region of the diagram not well populated by either sample. Interestingly, its position is very similar to the young EBs 2MJ0446+19 and NSVS 06507557 (see above). Given the dynamical processing that occurs during pre-main sequence evolution, we expect the youngest systems to have lower mass ratios. However, in all three cases the EBs are found in older (>20 Myr), sparser groups or in the field. While it is a small sample, we may be seeing the effect of an isolated environment on binary properties. J0552−0044 and the other systems may have formed in isolation, been ejected from their natal groups or drifted out when the groups lost their binding gas. In any case, J0552−0044 was not further disrupted and it survives to the present day on the outskirts of the 32 Ori Group.

Finally, as noted by Nefs et al. (2013), there is almost certainly

[9] https://www.astro.keele.ac.uk/jkt/debcat/

an observational bias towards equal-mass M+M binaries because of the steep mass–luminosity relationship for M dwarfs. Indeed, in the case of J0552−0044 we only detected the secondary through the velocity shift of its H α emission line, which was visible because of the enhanced chromospheric activity prevalent at lower masses.

4.2 Membership in the 32 Orionis Moving Group

Before a thorough comparison to evolutionary models, it is prudent to re-examine the proposed membership of J0552−0044 in the 32 Ori Group. B17 assigned J0552−0044 as a possible member based on its UCAC4 proper motion, 92 pc kinematic distance, colour–magnitude diagram (CMD) position and preliminary systemic velocity (20.9 ± 2.3 km s^{-1}). With an improved velocity and high-precision parallaxes and proper motions from the *Gaia* mission (Gaia Collaboration et al. 2018), we can more confidently claim membership in the group.

Of the 46 group members proposed in B17, only the L1 brown dwarf THOR 41 (=WISE J052857.69+090104.2; Burgasser et al. 2016) is not found in *Gaia* DR2. All but five members have parallaxes and proper motions. We plot the DR2 observables and heliocentric position (XYZ) and velocity (UVW) vectors for these stars and J0552−0044 in Fig. 18. While a full discussion of every group member in light of *Gaia* astrometry is outside the scope of this work, we can immediately reject THOR 33AB (5 arcsec binary) and THOR 34 (3 arcmin from 33AB) as members due to their significantly larger parallaxes (distance ∼38 pc). Their position and space motion make them probable members of the similarly-aged β Pictoris Moving Group (BPMG).[10] The remaining 32 Ori Group members in Fig. 18 form a coherent association in proper motion, parallax, radial velocity and colour–magnitude space, confirming their status as a true moving group.

J0552−0044 lies on the south-east periphery of the known membership, with a sky position, proper motion and W velocity component similar to the members THOR 16, 22, 23 and 26. Its DR2 distance is <2 pc from the group mean of 104.8 pc and its systemic velocity places it only 4.8 km s^{-1} (1.3σ) from the group mean of 19.5 ± 3.7 km s^{-1} (±1 s.d.; after removing the A3 outlier HD 35714, whose velocity is likely unreliable). Unsurprisingly, the system does not lie above the locus of (single) 32 Ori Group members in the CMD, as its SED is dominated by the M3.5 primary. Based on the distribution of members in Fig. 18 and radii consistent with ∼24 Myr isochrones, we conclude that J0552−0044 is a bona fide member of the 32 Ori Group. Following B17, we assign it the incremental membership number THOR 42.[11]

In their recent spectroscopic survey of the Orion OB1 association, Briceño et al. (2019) reported Li I λ6708 in J0552−0044, with an equivalent width (EW) of 123 mÅ. This was just above their estimated ∼100 mÅ detection limit. However, we did not detect Li I λ6708 in any of our WiFeS or Magellan spectra (EW $\leq$ 30 mÅ) and the EW distribution of 32 Ori Group members (Fig. 19) implies that an M3.5 star should not have detectable lithium at this age. Pre-main sequence evolutionary models predict that a 0.5 M$_\odot$ star should have fully depleted its surface lithium in ∼10 Myr. The non-detection of lithium in J0552−0044 is therefore necessary but insufficient evidence of membership in the group.

The mass (and hence luminosity) at which lithium remains unburnt in a stellar population is a sensitive function of age, which has been exploited in recent years to precisely age-date several groups and open clusters younger than $\lesssim$200 Myr, including the 32 Ori Group. B17 found a mean lithium depletion boundary (LDB, see Fig. 19) age of 23 ± 4 Myr, which relied on kinematic distances with errors of 8–30 per cent. This agreed with the isochronal age of 25 ± 5 Myr derived using the same distances, giving the final age for the group of 24 ± 4 Myr, which we adopt here.

4.3 Comparison to stellar evolutionary models

With its small mass ratio, well-determined parameters and young age, J0552−0044 permits precise comparisons to evolutionary models across a mass and age range poorly constrained by observations. In Figs. 20–23 we plot the fundamental parameters of the system compared to several widely-used model grids: BHAC15 (Fig. 20), the MESA Isochrones and Stellar Tracks (MIST v1.2, with $v/v_{\rm crit} = 0.4$; Choi et al. 2016; Dotter 2016, Fig. 21), the Pisa models of Tognelli et al. (2011) (extended down to 0.08 M$_\odot$; Fig. 22) and version 1.2S of the PARSEC models (Bressan et al. 2012, Fig. 23) which include modified $T-\tau$ relations from BT-Settl model atmospheres as surface boundary conditions (Chen et al. 2014). In all cases we adopt the solar-metallicity models.[12] The left panel of each figure shows that the components follow the expected gradient in the mass–radius diagram (MRD) and, with the exception of the PARSEC models, have radii close to those predicted for 24 Myr-old stars. The interpolated MRD ages for each component are given in Table 9. Uncertainties were calculated by a Monte Carlo simulation of 10^5 normal samples considering the tabled uncertainties in mass and radius. The components of J0552−0044 are therefore coeval within their 1σ uncertainties for the BHAC15 and Pisa models, but differ by 3σ (only 2.4 Myr) for MIST. The PARSEC v1.2S models imply significantly older ages (35–40 Myr) which are less coeval. However, in contrast to the other models, the PARSEC isochrones at these ages would predict luminosities close to those we have calculated for J0552−0044.

Given the fast rotation rate of the primary and the strong H α and X-ray emission we observed, we can assume both components are magnetically active. This activity is believed to produce stars with lower effective temperatures and inflated radii, either through magnetic fields reducing the efficiency of convection in the stellar interior, reduction of the effective radiating surface due to high spot coverage, or more likely a combination of both phenomena (e.g. Chabrier et al. 2007; MacDonald & Mullan 2014; Feiden & Chaboyer 2014; Somers & Pinsonneault 2015; Feiden 2016). Stassun et al. (2012) presented empirical correlations for quantifying the temperature decrement and radius inflation observed in <1 M$_\odot$ stars as a function of EW(H α) or the fractional X-ray luminosity. From both the (unresolved) $\log(L_{\rm X}/L_{\rm bol}) \approx -2.8$ we estimated in Sec. 3.3 and the primary's EW(H α) ≈ -5 Å, the relations predict a radius inflation of ∼14 per cent, with a corresponding temperature decrement of ∼6 per cent (∼200 K for the 3300 K primary). Assuming the age of J0552−0044 is not significantly older than ∼24 Myr, the excellent agreement between the measured radii and those predicted by the non-magnetic BHAC15, MIST and Pisa models for such an active system is challenging to explain.

The effects of adding magnetic fields are illustrated in Fig. 24, where we compare J0552−0044 to the models of Feiden (2016). These were computed assuming equipartition between the magnetic field pressure and gas pressure at a mean opacity of $\tau_{5000\,\text{Å}} =$

[10] Using *Gaia* astrometry and radial velocities from B17, the BANYAN-Σ tool (Gagné et al. 2018) returns membership probabilities of >99 per cent for the BPMG, with the balance of probabilities going to the young field.

[11] J0552−0044 was classified by B17 as a *possible* member and so not assigned a membership number in that study. As defined in B17 and adopted in recent works (e.g. BANYAN), the abbreviation THOR (= *TH*irty-two *OR*i) should not be confused with the distinct and much older Tucana–Horologium Association (often shortened to Tuc-Hor or THA).

[12] Note that the grids adopt slightly different helium (Y) and heavy element (Z) fractions for their solar metallicity models, with BHAC15 using (Y, Z) = (0.28, 0.0153), MIST using (0.2703, 0.0143) and Pisa using (0.253, 0.013). For PARSEC we adopt the (Y, Z) = (0.273, 0.014) tracks.

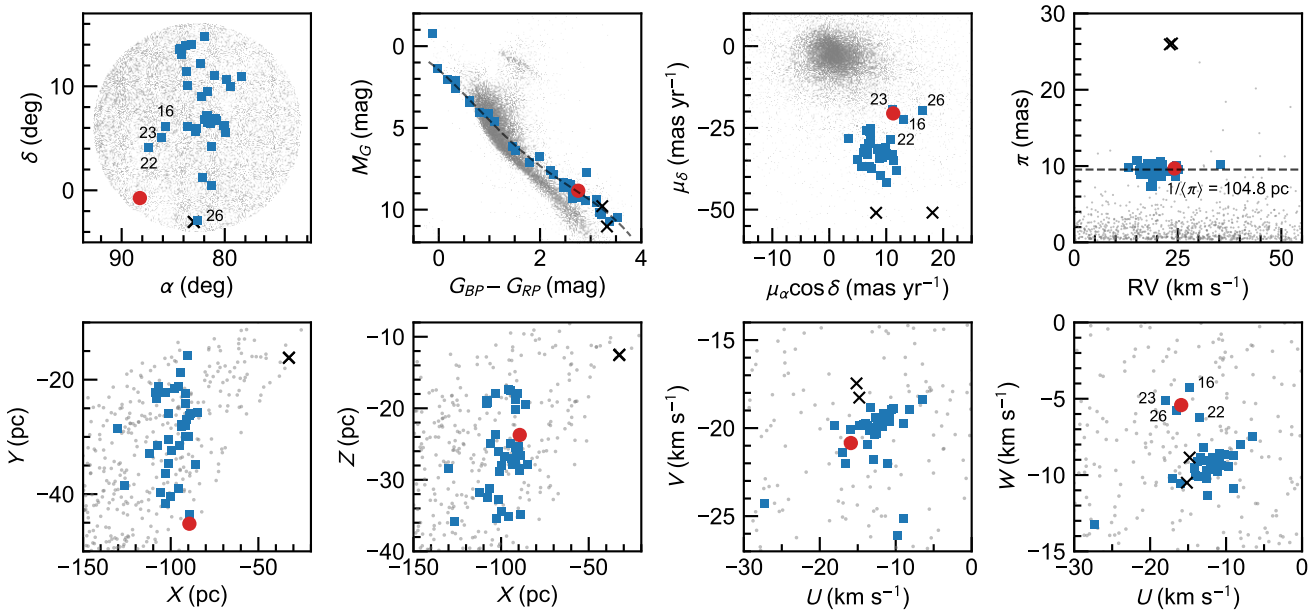


Figure 18. Top row: Proposed members of the 32 Ori Moving Group from B17 (blue squares) compared to J0552−0044 (red circle) in *Gaia* DR2 observables (left to right): sky position, photometry, proper motion and parallax (with radial velocities from B17). The two new non-members THOR 33 and 34 are shown as black crosses. Grey points are a random sample of 20 000 DR2 sources within 10° of 32 Ori itself with $\pi/\sigma_\pi > 10$. Only THOR 18 (SCR 05220606) is outside this 10° limit. A quartic polynomial has been fitted to members in the CMD to guide the eye. Bottom row: the same observables transformed to heliocentric XYZ positions and UVW velocities. Members mentioned in the text are labelled by their THOR number from B17.

Table 9. Isochronal ages of J0552−0044 in the mass–radius (MR) and Hertzsprung–Russell (HR) diagrams, with interpolated masses from the HRD.

Model	MRD age			HRD age			HRD mass			
	Primary (Myr)	Secondary (Myr)	Δt ($\lvert\sigma\rvert$)	Primary (Myr)	Secondary (Myr)	Δt ($\lvert\sigma\rvert$)	Primary ($M_\odot$)	ΔM (per cent)	Secondary ($M_\odot$)	ΔM (per cent)
BHAC15	25.4 ± 0.6	26.2 ± 0.6	1.0	9.9 ± 1.4	8.6 ± 0.9	0.8	0.24	−51	0.09	−58
MIST v1.2	24.5 ± 0.5	26.9 ± 0.5	3.2	9.4 ± 1.3	11.0[a]		0.25	−51	0.11	−49
Pisa	22.0 ± 0.5	22.4 ± 0.5	0.5	5.8 ± 0.7	~6.5		0.19	−62	<0.08[b]	−61
PARSEC v1.2S	35.1 ± 0.8	40.3 ± 0.7	4.6	29.2 ± 3.0	46.2 ± 4.4	3.2	0.44	−11	0.23	+12
Feiden (standard)	25.5 ± 0.6	26.3 ± 0.5	1.1	8.7 ± 1.2	~9.0		0.22	−55	<0.09[b]	−56
Feiden (magnetic)	31.8 ± 0.7	31.4 ± 0.6	0.4	16.2 ± 2.0	15.9 ± 1.6	0.1	0.31	−37	0.12	−41

[a] Temperature error bar falls outside the model grid. This will bias the age uncertainties.
[b] Secondary falls just outside the model grid. The mass is therefore an upper limit. Ages were estimated visually.

1 and adopt a surface magnetic field strength at each mass equal to the value at 10 Myr. Inhibition of convection by magnetic fields cools the stellar surface, slowing a star's contraction and making it appear older at fixed mass than the non-magnetic models. This is indeed what we see in Fig. 24, where the components of J0552−0044 remain coeval but have an inferred age of ~32 Myr. Note that the surface gas pressure increases as the star contracts, so we expect the field strengths to be larger in models calibrated at 20–30 Myr. In contrast, the non-magnetic Feiden (2016) isochrones yield ages of ~25 Myr, similar to the other models in Table 9.

Combining radius and mass to form the surface gravity, we see in the middle panels of Figs. 20–24 that all the models are able to maintain coevality in the $T_{\rm eff}$–$\log g$ plane, with BHAC15 and MIST slightly overestimating the system age and the Pisa models underestimating it. Again, the PARSEC and magnetic models imply older ages. However, the evolutionary tracks for 0.5 and 0.2 $M_\odot$ stars in these diagrams do not intersect the measured $\log g$ and $T_{\rm eff}$ (although the PARSEC tracks come close). The BHAC15, MIST and Pisa models all significantly underestimate the masses of the components. As extreme examples, consider the BHAC15 and Pisa models, which place the 0.5 $M_\odot$ primary component on or below the 0.2 $M_\odot$ track appropriate for the secondary.

Given the excellent agreement between the models and observations in the mass–radius plane, these discrepancies point to a problem with either the $T_{\rm eff}$ inferred from the SED fitting or the model temperature scales. The SED fit incorporates strong constraints on the component masses and radii from the joint modelling, which should be more accurate than those derived from single star spectral type–$T_{\rm eff}$ relations (e.g. Pecaut & Mamajek 2013; Herczeg & Hillenbrand 2014) applied to the primary star and transferred to the secondary through bandpass-dependent surface brightness ratios (see Gillen et al. 2017). Assuming the temperature scales of the BT-Settl and PHOENIX model atmospheres are correct, the BHAC15, MIST and Pisa tracks would need to be shifted approximately 300 K cooler to match the observations (Fig. 25). This is similar to the ~200 K decrement predicted from the Stassun et al. (2012) activity relations (which also used non-magnetic models). The effect is also visible in the mass–radius plane, where the models predict lower-than-observed radii at fixed mass and luminosity, a consequence of the overestimated temperatures. Temperature shifts of similar size and direction have been reported across a variety of young, low-mass EBs and models (e.g. Kraus et al. 2015; David et al. 2016a,b; Gillen et al. 2017; David et al. 2019; Simon et al. 2019), suggesting that the models themselves are to blame. With cooler temperatures but uninflated radii, J0552−0044 is the inverse of the similarly-aged MML 53, where

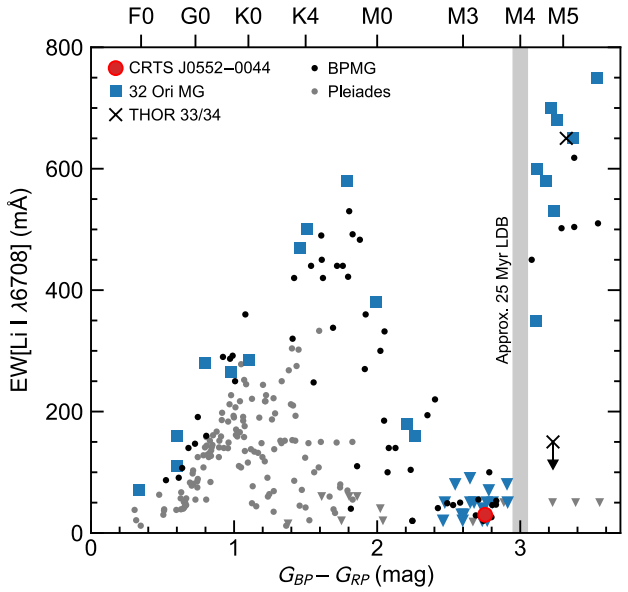


Figure 19. Li I λ6708 equivalent widths for members of the 32 Ori Group, the β Pic Moving Group (BPMG) and the Pleiades. Upper limits are denoted by arrows. We detected no Li I in J0552−0044 (EW $\leq$ 30 mÅ). The approximate location of the 25 Myr Lithium Depletion Boundary (LBD) observed in the 32 Ori Group and BPMG is given by the shaded region.

Gómez Maqueo Chew et al. (2019) reported its components were larger but not cooler than predicted by non-magnetic evolutionary models.

The disagreement between theory and observation is even starker when moving to the more commonly-used H–R diagram (HRD) of $T_{\rm eff}$ versus log L (Figs. 20–24; right hand panels). Placing the components of J0552−0044 on this diagram we infer (generally coeval) ages 2–4 times younger than from the mass–radius diagram (see Table 9). Again, shifting the models 300–350 K cooler (with a corresponding decrease in the Stefan–Boltzmann luminosity) does much to ameliorate the discrepancies (Fig. 25). However, this is unlikely to completely solve the problem, since the models cannot be shifted purely in $T_{\rm eff}$. Lower temperatures mean less energy radiated from the surface, slowing the contraction rate and changing the radius and luminosity at a given age (Kraus et al. 2015). The PARSEC models show minimal difference between their MRD and HRD ages but are not as coeval as the other grids. However, they are the only models to show any coevality *between* the observed planes. The components of J0552−0044 can be well fitted in all three panels by a 35–40 Myr isochrone (dashed lines in Fig. 23).

As with the $T_{\rm eff}$–log g diagram, the over-predicted temperatures mean the models predict much lower masses for J0552−0044 than we found from the orbital solution. The BHAC15, MIST, Pisa and non-magnetic Feiden models all underestimate the dynamical masses by 50–60 per cent (Table 9). Similar trends have been reported in the literature for other young systems with well-established masses (e.g. Hillenbrand & White 2004; Kraus et al. 2015; Simon et al. 2019). The magnetic models do slightly better (−40 per cent), but only the PARSEC tracks come close to the true values; underestimating the primary mass by only ∼10 per cent and overestimating the secondary by a similar amount.

It is evident from these comparisons that none of the models are able to simultaneously predict the mass, radius, temperature and luminosity of J0552−0044 at the assumed 24 Myr age of the 32 Ori Group. The BHAC15, MIST and Pisa models can reproduce the expected radii in the MRD, but require a shift in their temperature scales of ∼300 K to match the HRD positions of the components. The PARSEC models predict significantly older ages in both the MRD and HRD, but are better able to replicate the observed masses without a temperature shift. These models include ad hoc corrections to the BT-Settl $T-\tau$ surface boundary conditions at the lowest temperatures to better match the observed mass–radius relation of low-mass dwarfs (Chen et al. 2014). While this has been suggested as an over-correction in the pre-main sequence regime (i.e. if the adjustments are necessary due to missing opacities which are more important at higher gravities, e.g. Kraus et al. 2015), perhaps by the age of the 32 Ori Group, J0552−0044 is sufficiently close to the main sequence for this to be no longer the case.

5 CONCLUSION

We have presented a full characterization of the young, low-mass eclipsing binary CRTS J055255.7−004426 (=THOR 42), which we confirm is a member of the ∼24 Myr-old 32 Orionis Moving Group. We have modelled the light and radial velocity curves to derive precise system parameters, yielding component masses and radii of 0.497 ± 0.005 and 0.205 ± 0.002 $M_\odot$, and 0.659 ± 0.003 and 0.424 ± 0.002 $R_\odot$, respectively (mass and radius uncertainties of 1 per cent and 0.5 per cent). With components spanning the fully-convective boundary for M dwarfs, THOR 42 provides a stringent test of evolutionary models near the start of the main sequence, which is currently not well constrained by observations.

Surprisingly for such a tight (0.859 d period), synchronized ($v \sin i$ = 38 km s^{-1}) system, the radii we measure are no larger than those predicted by most non-magnetic models for a 20–25 Myr star (i.e. no anomalous inflation), in excellent agreement with the canonical age of the 32 Ori Group. However, none of the models can simultaneously predict the observed mass, radius, temperature and luminosity of the components at this age. Specifically, the H–R diagram position of THOR 42 would lead to 50–60 per cent smaller masses and 2–4 times younger ages being estimated from most model tracks and isochrones. The latest PARSEC models (Chen et al. 2014) preserve coevality across the mass–radius and H–R diagrams and come closest to replicating the dynamical masses of the system, but require a significantly older age of 35–40 Myr. A re-examination of the 32 Ori Group's isochronal and lithium depletion ages in light of *Gaia* parallaxes is necessary to confirm whether this older age can be supported. During this work we also found that two proposed 32 Ori Group members; THOR 33AB and 34, are in fact more likely members of the β Pictoris Moving Group.

The discovery and characterization of more high-precision touchstone systems like THOR 42 at a range of masses and ages is necessary to calibrate the models across the entire pre-main sequence. Nearby young moving groups like 32 Orionis and the older subgroups of the Sco-Cen OB association will no doubt be especially fertile grounds for such work.

ACKNOWLEDGEMENTS

We thank Pierre Maxted, Edward Gillen, Andrew Casey and Melissa Ness for fruitful discussions regarding model fitting, and the referee for a prompt and thorough review of the manuscript. We acknowledge the traditional owners of the land on which SSO is located, the Gamilaraay people, and pay our respects to their elders past and present. We also acknowledge the generosity of the indigenous Hawaiian people to allow observations from Haleakalā.

SJM acknowledges the support of a Vice Chancellor's Postdoctoral Fellowship at the University of New South Wales Canberra and a visiting fellowship at the Australian National University. CPMB acknowledges support from the European Research Council (ERC) under the European Union's Horizon 2020 research and innovation programme (grant agreement no. 682115).

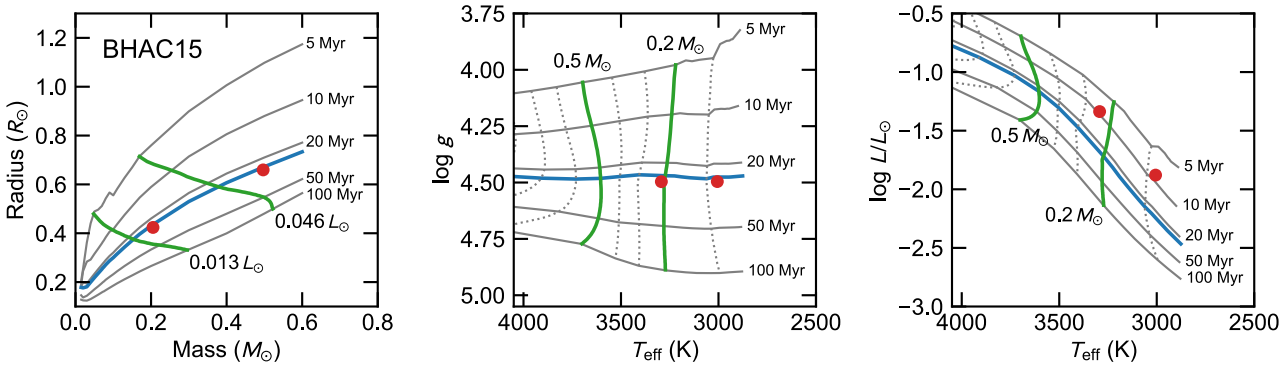


Figure 20. Comparison of J0552−0044 against 5, 10, 20, 50 and 100 Myr solar-metallicity Baraffe et al. (2015) models. From left to right are the mass–radius, $T_{\rm eff}$–log g and $T_{\rm eff}$–luminosity (H–R diagram) planes. The thick blue line in each panel is the 24 Myr isochrone appropriate for members of the 32 Ori Group, while the thick green lines in the $T_{\rm eff}$–log g and $T_{\rm eff}$–luminosity plots are evolutionary tracks for the 0.2 and 0.5 $M_\odot$ components of J0552−0044. The green lines in the mass–radius plot are isolums at the 0.046 and 0.013 $L_\odot$ we find for the primary and secondary components, respectively.

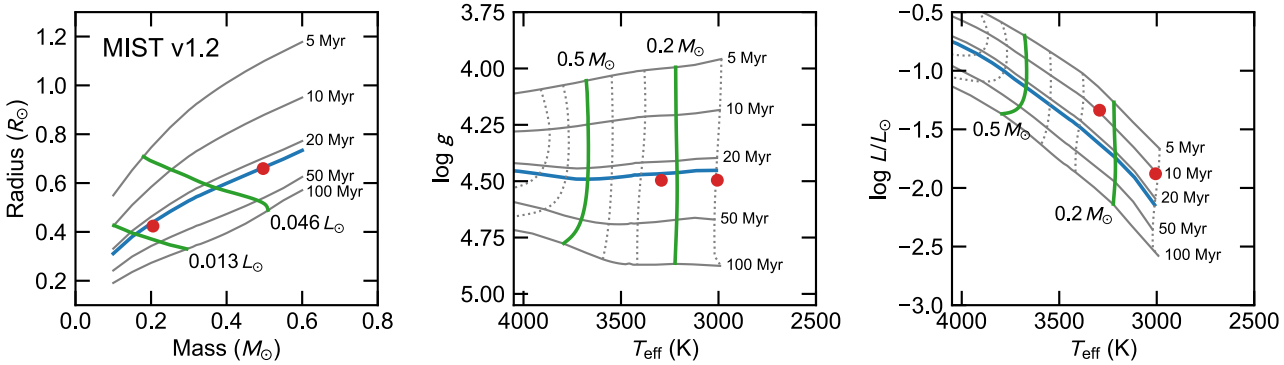


Figure 21. As in Fig. 20, but for MIST v1.2 models ($v/v_{\rm crit}$ = 0.4; Dotter 2016; Choi et al. 2016).

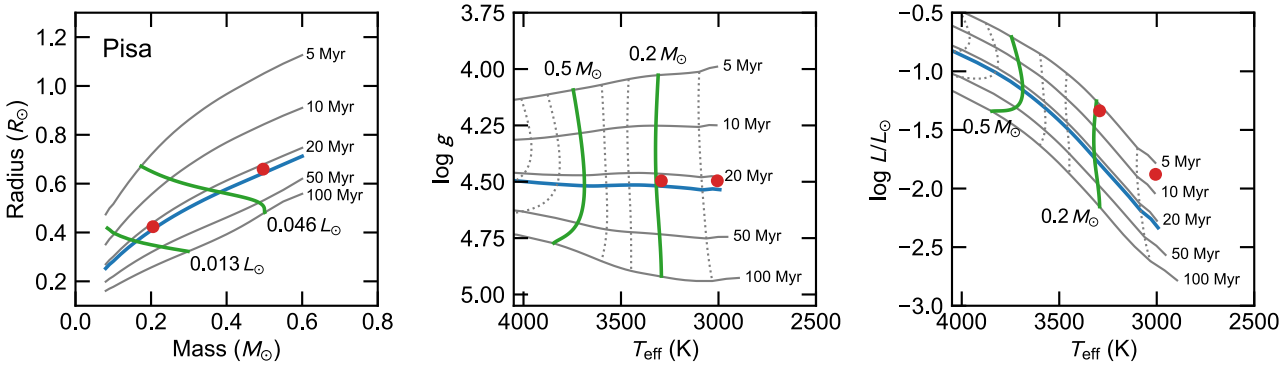


Figure 22. As in Fig. 20, but for Pisa models (Tognelli et al. 2011), extended down to 0.08 $M_\odot$.

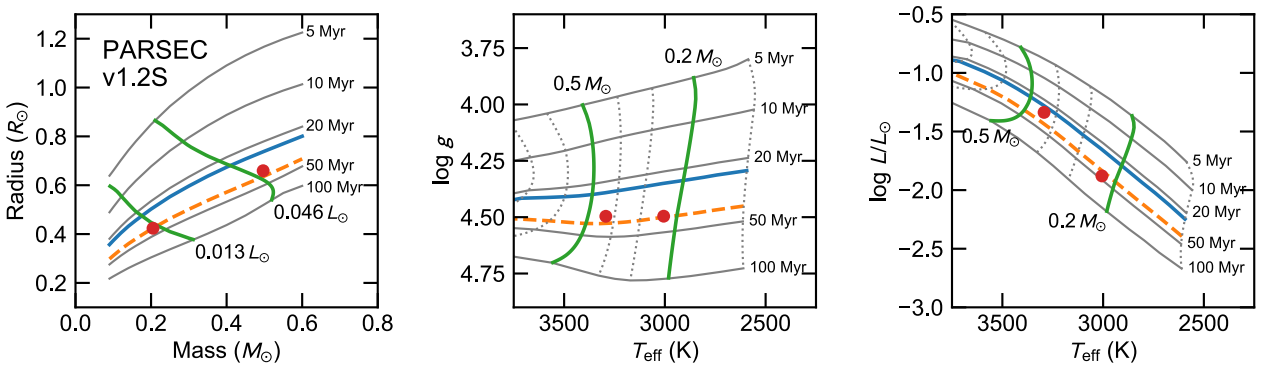


Figure 23. As in Fig. 20, but for PARSEC v1.2S models (Bressan et al. 2012; Chen et al. 2014). The dashed yellow line in each panel is the 40 Myr isochrone.

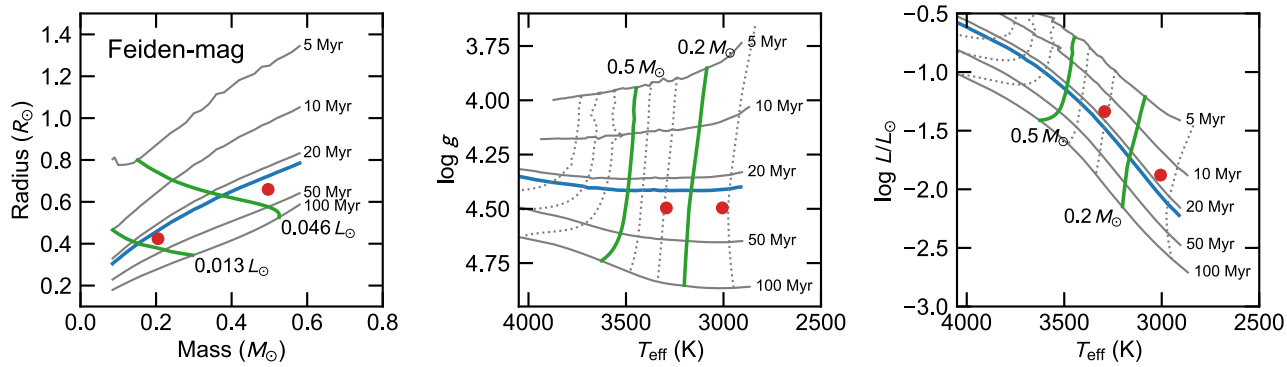


Figure 24. As in Fig. 20, but for the solar-metallicity magnetic models of Feiden (2016).

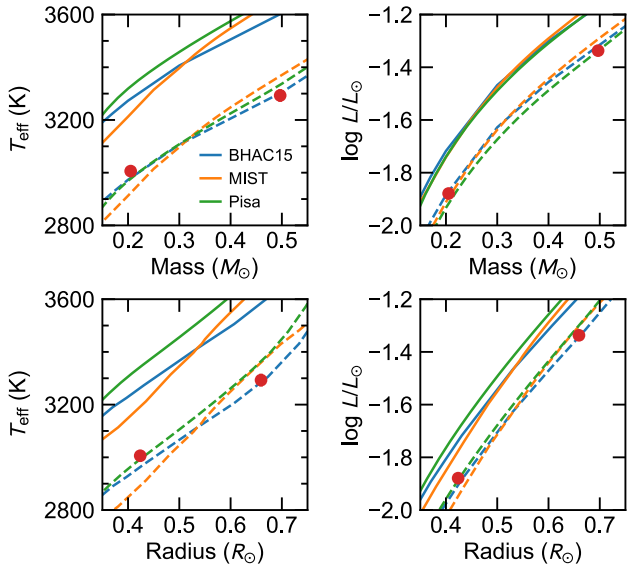


Figure 25. Temperatures and luminosities of 24 Myr BHAC15, MIST and Pisa magnetic models as a function of mass and radius (solid lines). The red points are our measurements for J0552−0044. Dashed lines show the effect of a simple shift in $T_{\rm eff}$ (or corresponding shift in log L) of −300 K (BHAC15, MIST) or −350 K (Pisa) at fixed mass and radius.

This work includes data gathered with the 6.5 meter Magellan Telescopes located at Las Campanas Observatory, Chile. Australian access to the Magellan Telescopes was supported through the National Collaborative Research Infrastructure Strategy of the Australian Federal Government.

This work has made use of observations from the Las Cumbres Observatory Global Telescope (LCOGT) network, granted through guaranteed time of the Australian National University.

Part of this research was carried out at the Jet Propulsion Laboratory, California Institute of Technology, under a contract with NASA.

This material is based upon work supported by the National Science Foundation Graduate Research Fellowship Program under Grant No. (DGE-1746045). Any opinions, findings, and conclusions or recommendations expressed in this material are those of the authors and do not necessarily reflect the views of the National Science Foundation.

This work has made use of data from the European Space Agency (ESA) mission *Gaia* (https://www.cosmos.esa.int/gaia), processed by the *Gaia* Data Processing and Analysis Consortium (DPAC, https://www.cosmos.esa.int/web/gaia/dpac/consortium). Funding for the DPAC has been provided by national institutions, in particular the institutions participating in the *Gaia* Multilateral Agreement.

The national facility capability for SkyMapper has been funded through ARC LIEF grant LE130100104 from the Australian Research Council, awarded to the University of Sydney, the Australian National University, Swinburne University of Technology, the University of Queensland, the University of Western Australia, the University of Melbourne, Curtin University of Technology, Monash University and the Australian Astronomical Observatory. SkyMapper is owned and operated by The Australian National University's Research School of Astronomy and Astrophysics.

This work includes data collected by the *TESS* mission, which are publicly available from the Mikulski Archive for Space Telescopes (MAST). Funding for the *TESS* mission is provided by NASA's Science Mission directorate.

Software: PYTHON (v3.7.2), IPYTHON (v6.5.0; Pérez & Granger 2007), ASTROPY (v3.2.1; Astropy Collaboration et al. 2013), ELLC (v1.8.4; Maxted 2016), ELEANOR (v0.2.4; Feinstein et al. 2019), EMCEE (v2.2.1; Foreman-Mackey et al. 2013), PYASTRONOMY (v0.13.0, https://github.com/sczesla/PyAstronomy), MATPLOTLIB (v3.1.1; Hunter 2007), SCIPY (v1.3.0; http://scipy.org), NUMPY (v1.17.0; Oliphant 2006).

REFERENCES

Aguado D. S., et al., 2019, ApJS, 240, 23
Allard F., Homeier D., Freytag B., 2012, Royal Society of London Philosophical Transactions Series A, 370, 2765
Andersen J., 1991, A&ARv, 3, 91
Astropy Collaboration et al., 2013, A&A, 558, A33
Bailer-Jones C. A. L., Rybizki J., Fouesneau M., Mantelet G., Andrae R., 2018, AJ, 156, 58
Baraffe I., Homeier D., Allard F., Chabrier G., 2015, A&A, 577, A42
Bastian N., Covey K. R., Meyer M. R., 2010, ARA&A, 48, 339
Bate M. R., 2000, MNRAS, 314, 33
Bate M. R., Bonnell I. A., Bromm V., 2002, MNRAS, 336, 705
Bell C. P. M., Naylor T., Mayne N. J., Jeffries R. D., Littlefair S. P., 2013, MNRAS, 434, 806
Bell C. P. M., Murphy S. J., Mamajek E. E., 2017, MNRAS, 468, 1198
Bernstein R., Shectman S. A., Gunnels S. M., Mochnacki S., Athey A. E., 2003, in Iye M., Moorwood A. F. M., eds, Society of Photo-Optical Instrumentation Engineers (SPIE) Conference Series Vol. 4841, Proc. SPIE. pp 1694–1704, doi:10.1117/12.461502
Bertin E., 2011, in Evans I. N., Accomazzi A., Mink D. J., Rots A. H., eds, Astronomical Society of the Pacific Conference Series Vol. 442, Astronomical Data Analysis Software and Systems XX. p. 435
Bessell M., Murphy S., 2012, PASP, 124, 140
Bessell M., Bloxham G., Schmidt B., Keller S., Tisserand P., Francis P., 2011, PASP, 123, 789
Bohlin R. C., Gordon K. D., Tremblay P. E., 2014, PASP, 126, 711
Boller T., Freyberg M. J., Trümper J., Haberl F., Voges W., Nandra K., 2016, A&A, 588, A103
Boyajian T. S., et al., 2012, ApJ, 757, 112

Bressan A., Marigo P., Girardi L., Salasnich B., Dal Cero C., Rubele S., Nanni A., 2012, MNRAS, 427, 127
Briceño C., et al., 2019, AJ, 157, 85
Brown T. M., et al., 2013, PASP, 125, 1031
Browning M. K., Basri G., Marcy G. W., West A. A., Zhang J., 2010, AJ, 139, 504
Burgasser A. J., et al., 2016, ApJ, 820, 32
Ćakırlı Ö., Ibanoğlu C., 2010, MNRAS, 401, 1141
Cardelli J. A., Clayton G. C., Mathis J. S., 1989, ApJ, 345, 245
Chabrier G., Baraffe I., 1997, A&A, 327, 1039
Chabrier G., Gallardo J., Baraffe I., 2007, A&A, 472, L17
Chambers K. C., et al., 2016, arXiv e-prints astro-ph:1612.05560, p. arXiv:1612.05560
Chen Y., Girardi L., Bressan A., Marigo P., Barbieri M., Kong X., 2014, MNRAS, 444, 2525
Choi J., Dotter A., Conroy C., Cantiello M., Paxton B., Johnson B. D., 2016, ApJ, 823, 102
Claret A., Bloemen S., 2011, A&A, 529, A75
Cohen M., Wheaton W. A., Megeath S. T., 2003, AJ, 126, 1090
David T. J., et al., 2016a, AJ, 151, 112
David T. J., Hillenbrand L. A., Cody A. M., Carpenter J. M., Howard A. W., 2016b, ApJ, 816, 21
David T. J., Hillenbrand L. A., Gillen E., Cody A. M., Howell S. B., Isaacson H. T., Livingston J. H., 2019, ApJ, 872, 161
Dopita M., Hart J., McGregor P., Oates P., Bloxham G., Jones D., 2007, Ap&SS, 310, 255
Dotter A., 2016, ApJS, 222, 8
Drake A. J., et al., 2014, ApJS, 213, 9
Eggleton P. P., 1983, ApJ, 268, 368
Evans D. W., et al., 2018, A&A, 616, A4
Feiden G. A., 2015, in Rucinski S. M., Torres G., Zejda M., eds, Astronomical Society of the Pacific Conference Series Vol. 496, Living Together: Planets, Host Stars and Binaries. p. 137 (arXiv:1506.02715)
Feiden G. A., 2016, A&A, 593, A99
Feiden G. A., Chaboyer B., 2014, ApJ, 789, 53
Feinstein A. D., et al., 2019, PASP, 131, 094502
Fleming T. A., Gioia I. M., Maccacaro T., 1989, ApJ, 340, 1011
Fleming T. A., Molendi S., Maccacaro T., Wolter A., 1995, ApJS, 99, 701
Flesch E. W., 2016, Publ. Astron. Soc. Australia, 33, e052
Foreman-Mackey D., Hogg D. W., Lang D., Goodman J., 2013, PASP, 125, 306
Gagné J., et al., 2018, ApJ, 856, 23
Gaia Collaboration et al., 2018, A&A, 616, A1
Gillen E., Hillenbrand L. A., David T. J., Aigrain S., Rebull L., Stauffer J., Cody A. M., Queloz D., 2017, ApJ, 849, 11
Gómez Maqueo Chew Y., et al., 2019, A&A, 623, A23
Goodman J., Weare J., 2010, Communications in Applied Mathematics and Computational Science, Vol.~5, No.~1, p.~65-80, 2010, 5, 65
Goodwin S. P., Kroupa P., Goodman A., Burkert A., 2007, in Reipurth B., Jewitt D., Keil K., eds, Protostars and Planets V. University of Arizona Press, p. 133 (arXiv:astro-ph/0603233)
Gray D. F., 2008, The Observation and Analysis of Stellar Photospheres. Cambridge University Press, Cambridge, UK
Hebb L., Wyse R. F. G., Gilmore G., Holtzman J., 2006, AJ, 131, 555
Hebb L., et al., 2010, A&A, 522, A37
Hebb L., Cegla H. M., Stassun K. G., Stempels H. C., Cargile P. A., Palladino L. E., 2011, A&A, 531, A61
Heinze A. N., et al., 2018, AJ, 156, 241
Henden A. A., 2019, JAAVSO, 47, 130
Henry T. J., Subasavage J. P., Brown M. A., Beaulieu T. D., Jao W., Hambly N. C., 2004, AJ, 128, 2460
Herczeg G. J., Hillenbrand L. A., 2014, ApJ, 786, 97
Hillenbrand L. A., White R. J., 2004, ApJ, 604, 741
Hunter J. D., 2007, Computing in Science & Engineering, 9, 90
Husser T. O., Wende-von Berg S., Dreizler S., Homeier D., Reiners A., Barman T., Hauschildt P. H., 2013, A&A, 553, A6
Jayasinghe T., et al., 2019, MNRAS, 486, 1907
Karim M. T., et al., 2016, AJ, 152, 198
Kelson D. D., 2003, PASP, 115, 688
Kelson D. D., Illingworth G. D., van Dokkum P. G., Franx M., 2000, ApJ, 531, 184
Kipping D. M., 2013, MNRAS, 435, 2152
Kirkpatrick J. D., Henry T. J., McCarthy Jr. D. W., 1991, ApJS, 77, 417
Kochanek C. S., et al., 2017, PASP, 129, 104502
Kraus A. L., Cody A. M., Covey K. R., Rizzuto A. C., Mann A. W., Ireland M. J., 2015, ApJ, 807, 3
Lacy C. H. S., Fekel F. C., Pavlovski K., Torres G., Muterspaugh M. W., 2016, AJ, 152, 2
Lallement R., et al., 2018, A&A, 616, A132
Lee C.-H., 2015, MNRAS, 454, 2946
Lodieu N., et al., 2015, A&A, 584, A128
López-Morales M., Ribas I., 2005, ApJ, 631, 1120
Luhman K. L., Stauffer J. R., Muench A. A., Rieke G. H., Lada E. A., Bouvier J., Lada C. J., 2003, ApJ, 593, 1093
MacDonald J., Mullan D. J., 2014, ApJ, 787, 70
Mainzer A., et al., 2011, ApJ, 731, 53
Mamajek E. E., 2007, in Elmegreen B. G., Palous J., eds, IAU Symposium Vol. 237, Triggered Star Formation in a Turbulent ISM. pp 442–442, doi:10.1017/S174392130700230X
Mamajek E. E., 2009, in T. Usuda, M. Tamura, & M. Ishii ed., American Institute of Physics Conference Series Vol. 1158, Exoplanets and Disks: their formation and diversity: Proceedings of the International Conference. pp 3–10 (arXiv:0906.5011)
Mamajek E. E., et al., 2015, arXiv e-prints astro-ph:1510.07674, p. arXiv:1510.07674
Mann A. W., von Braun K., 2015, PASP, 127, 102
Mann A. W., et al., 2015, in 18th Cambridge Workshop on Cool Stars, Stellar Systems, and the Sun. pp 80–104 (arXiv:1410.6807)
Maxted P. F. L., 2016, A&A, 591, A111
Maxted P. F. L., Hutcheon R. J., 2018, A&A, 616, A38
McCully C., Volgenau N. H., Harbeck D.-R., Lister T. A., Saunders E. S., Turner M. L., Siiverd R. J., Bowman M., 2018, in Proc. SPIE. p. 107070K (arXiv:1811.04163), doi:10.1117/12.2314340
Murphy S. J., Lawson W. A., 2015, MNRAS, 447, 1267
Murphy S. J., Mamajek E. E., Bell C. P. M., 2018, MNRAS, 476, 3290
Nefs S. V., et al., 2013, MNRAS, 431, 3240
Nidever D. L., Marcy G. W., Butler R. P., Fischer D. A., Vogt S. S., 2002, ApJS, 141, 503
Oliphant T. E., 2006, A guide to NumPy. Trelgol Publishing USA
Onken C. A., et al., 2019, Publ. Astron. Soc. Australia, 36, e033
Papageorgiou A., Catelan M., Christopoulou P.-E., Drake A. J., Djorgovski S. G., 2018, ApJS, 238, 4
Parviainen H., Aigrain S., 2015, MNRAS, 453, 3821
Pecaut M. J., Mamajek E. E., 2013, ApJS, 208, 9
Pecaut M. J., Mamajek E. E., 2016, MNRAS, 461, 794
Pérez F., Granger B. E., 2007, Computing in Science and Engineering, 9, 21
Reid I. N., Hawley S. L., Gizis J. E., 1995, AJ, 110, 1838
Reiners A., 2007, A&A, 467, 259
Ribas I., 2003, A&A, 398, 239
Ricker G. R., et al., 2015, Journal of Astronomical Telescopes, Instruments, and Systems, 1, 014003
Shappee B. J., et al., 2014, ApJ, 788, 48
Shortridge K., 1993, in R. J. Hanisch, R. J. V. Brissenden, & J. Barnes ed., Astronomical Society of the Pacific Conference Series Vol. 52, Astronomical Data Analysis Software and Systems II. p. 219
Simon M., et al., 2019, ApJ, 884, 42
Skrutskie M. F., et al., 2006, AJ, 131, 1163
Somers G., Pinsonneault M. H., 2015, ApJ, 807, 174
Southworth J., 2015, in Rucinski S. M., Torres G., Zejda M., eds, Astronomical Society of the Pacific Conference Series Vol. 496, Living Together: Planets, Host Stars and Binaries. p. 164 (arXiv:1411.1219)
Stassun K. G., Kratter K. M., Scholz A., Dupuy T. J., 2012, ApJ, 756, 47
Stassun K. G., Feiden G. A., Torres G., 2014, New Astron. Rev., 60, 1
Stauffer J. R., Hartmann L. W., Prosser C. F., Randich S., Balachandran S., Patten B. M., Simon T., Giampapa M., 1997, ApJ, 479, 776
Sterzik M. F., Durisen R. H., 1995, A&A, 304, L9
Tognelli E., Prada Moroni P. G., Degl'Innocenti S., 2011, A&A, 533, A109
Tonry J. L., et al., 2012, ApJ, 750, 99
Tonry J. L., et al., 2018a, PASP, 130, 064505
Tonry J. L., et al., 2018b, ApJ, 867, 105
Torres G., Ribas I., 2002, ApJ, 567, 1140
Torres G., Andersen J., Giménez A., 2010, A&ARv, 18, 67
Vanderspek R., Doty J., Fausnaugh M., Villasenor J., Jenkins J. M., Berta-Thompson Z. K., Burke C. J., Ricker G. R., 2018, v0.1, TESS Instrument Handbook. NASA

Watson C. L., Henden A. A., Price A., 2006, Society for Astronomical Sciences Annual Symposium, 25, 47
West A. A., et al., 2011, AJ, 141, 97
White R. J., Basri G., 2003, ApJ, 582, 1109
Wolf C., et al., 2018, Publ. Astron. Soc. Australia, 35, e010
Wright E. L., et al., 2010, AJ, 140, 1868
Zahn J. P., 1977, A&A, 500, 121

This paper has been typeset from a TEX/LATEX file prepared by the author.